2019

Studying Category-Based Visual Attention and Mental Imagery in the Human Brain Using Local Field Potentials

Zahraa Naji Sabra
Medical University of South Carolina

Follow this and additional works at: https://medica-musc.researchcommons.org/theses

Recommended Citation

Studying Category-Based Visual Attention and Mental Imagery in the Human Brain Using Local Field Potentials

by

Zahraa Naji Sabra

A dissertation submitted to the faculty of the Medical University of South Carolina in partial fulfillment of the requirements for the degree of Doctor of Philosophy in the College of Graduate Studies.

Department of Neurosciences

2019

Approved by:

Chairman, Advisory Committee

_____

Thomas Naselaris

_____

Leonardo Bonilha

_____

Nathan Rowland

_____

Prakash Kara

_____

Thomas Jhou

DEDICATION

To whom all our work belongs, because its start and end are to him.

وَمَا تَوْفِيقِي إِلاَّ بِاللَّهِ عَلَيْهِ تَوَكَّلْتُ وَإِلَيْهِ أُنِيبُ

ACKNOWLEDGEMENTS

TABLE OF CONTENTS

LIST OF TABLES

LIST OF FIGURES

LIST OF ABBREVIATIONS

ECoG   Electrocorticography

FFA   Fusiform Face Area

fMRI   functional Magnetic Resonance Imaging

LFP   Local Field potential

MEG   Magnetoencephalography

MI   Mental Imagery

PC   Principal Component

PCA   Principal Component Analysis

PPA   Parahippocampal Place Area

PSD   Power Spectral Density

V1   Primary visual cortex

V2   Secondary visual cortex

ZAHRAA NAJI SABRA. Studying Category-Based Visual Attention and Mental Imagery in the Human Brain Using Local Field Potentials. (Under the direction of THOMAS NASELARIS).

ABSTRACT

Cerebral processing of visual stimuli is characterized by a complex circuitry involved in processing visual inputs while simultaneously contextualizing, categorizing or modulating these inputs by higher-order cortical centers. The sensory input and the cognitive control over this input can potentially be differentiated spatially, i.e. different brain regions, or spectrally, i.e. different frequencies of neuronal activity. In this work, we used object-category based visual tasks to investigate the spectral and spatial patterns of encoding of visual inputs and cognitive control at the level of visual attention and mental imagery using local field potentials in human subjects across widely distributed recording sites and a broad frequency spectrum(1-100Hz). Using PCA, we demonstrate that during a task involving both visual attention to an object category with varied observed category a broadband, and two narrowband low-frequency explained the main variance in the data. When comparing response to attended versus seen categories, we did not observe a spatial difference in location of encoding sites, but using decoding models, the broadband signal decodes vision better than attention in visual cortex and vision and attention equally in the temporal lobe. However, narrowband delta-theta decodes the best for both vision and attention, and alpha-beta differentially decodes for attention better than vision. Using an alternate task that involves image memorization, imagery, and passive viewing, we demonstrate that the main power spectral modulation among those mental states are represented by a broadband, gamma band, and low-frequency band. Encoding sites were similarly spatially widely distributed. Decoding models showed that

gamma band predicts attentive viewing and mental imagery with best accuracy. Both broadband and low frequency band accurately decode for passive and attentive viewing. Our findings demonstrate that encoding of vision, attention and mental imagery is not dependent on a single spectral domain and optimal decoding of visual processes should consider the co-contribution of narrowband and broadband spectral patterns to account for the different co-occurring top-down and bottom-up processes. Therefore, although gamma-significantly studied in vision-is involved in visual working-memory tasks, both broadband and low-frequency narrowband patterns of neuronal activity co-participate in visual processing in the context of object-based visual attention and mental imagery.

CHAPTER ONE

INTRODUCTION

1.1. Definitions

1.1.1. Visual receptive field

The visual receptive field for a certain neuron corresponds to the components and/or location of the visual field that elicit neuronal activity in this neuron. The complexity and size of the receptive field increases when moving from primary visual cortex (V1) to higher cognitive visual regions (**Figure 1.1**).
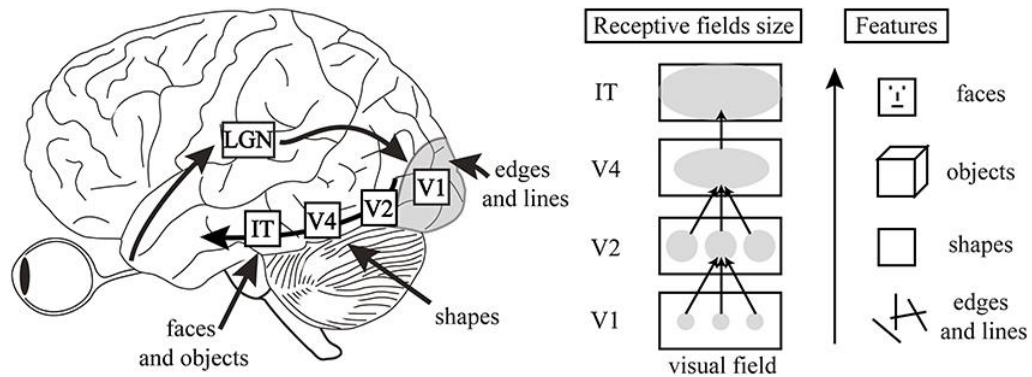
Figure 1.1. Size and complexity of receptive field along the hierarchy of visual cognitive processing

Adapted from (Herzog and Clarke, 2014). The figure illustrates how the size and complexity of receptive fields increase when going from primary visual cortex (V1) to higher visual brain regions (IT: Inferior temporal). In parallel, the complexity of features extracted from stimulus within the receptive field also increases along the hierarchy of visual cognitive processing (V1→ V2 → V4 → IT) .

1.1.2. Spatial distribution of neuronal activity

By spatial distribution we refer to anatomical locations within the MNI (Montreal Neurological Institute) space of the studied recording sites on a normalized brain.

1.1.3. Spectral domain representation of neuronal activity

The spectral domain of neuronal activity is the frequency domain representation of a time series recording of neuronal activity that shows the power at each represented frequency value. The spectral representation of neuronal response to a stimulus is used to compare the responses of a recording site to various stimuli by studying modulations in power across different frequencies.

1.1.4. Spectral pattern

The spectral pattern refers to the form of the neuronal response signal in the frequency domain. Two major spectral patterns could be noticed when studying stimulus-induced neuronal activity: broadband and narrowband spectral patterns.

1.1.5. Narrowband modulation in the spectral domain

In the frequency domain, when comparing the modulation of power over a frequency range between two or more conditions, a narrowband increase/decrease of power appears as a peak over a narrow range of frequencies. This narrowband spectral pattern could take place in the low frequency (< 30Hz) or in the high frequency (>30Hz) bands. **Figure 1.2A** and **Figure 1.3** show an example of a narrowband peak in the time-frequency spectrograms and in power spectra respectively.

1.1.6. Broadband modulation in the spectral domain

A broadband pattern of spectral modulation represents a generalized increase/decrease of power spanning a wide range of frequencies. This broadband modulation could span the whole range of the studied frequencies. **Figure 1.2B** and **Figure 1.3** shows an example of a broadband change in the time-frequency spectrograms and in power spectra respectively.
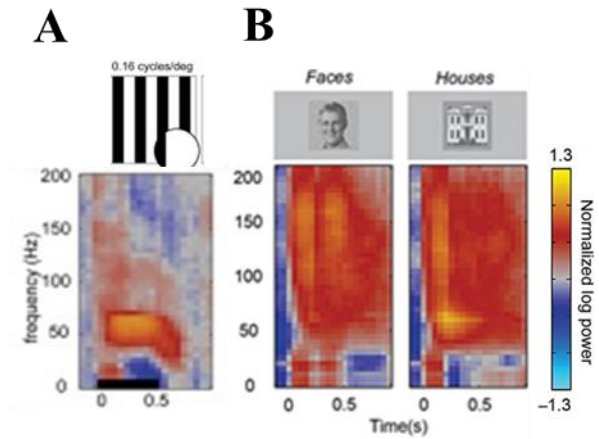
Figure 1.2. Example of broadband and narrowband spectral modulation patterns

(A) Time-frequency plot showing an increase in power in early visual cortex for the duration of onset (0.5 sec) of a grating stimulus, and demonstrating a narrowband response within the gamma band. **(B)** Time-frequency plots showing a broadband increase in power over a wide range of frequency after the onset of faces and houses stimuli in a recording site from the ventral temporal cortex. adapted from (Hermes et al., 2015)
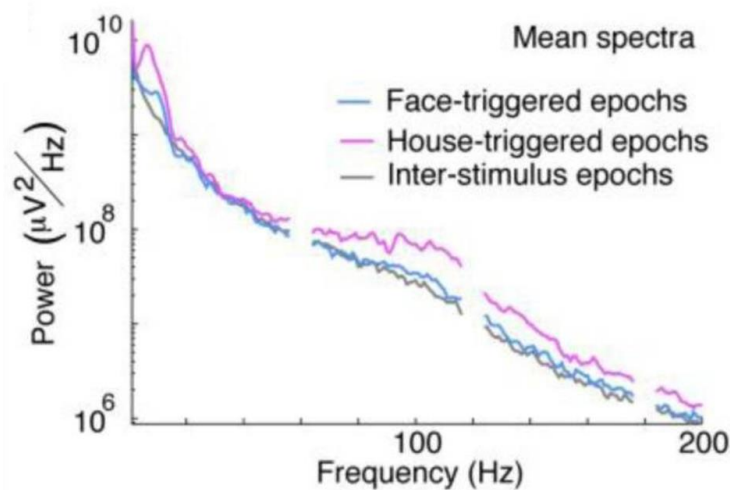
Figure 1.3. Power spectra showing broadband and narrowband modulation patterns

Power spectral plot showing the mean frequency representation of the response of local field potential recording site from the parahippocampus of human brain to stimuli displayed on the screen for 0.5 sec, and featuring house (pink), face (blue), and inter-stimulus interval (gray). Broadband increase of response to house-triggered epochs was clearly seen in the gamma band when compared to responses to face and inter-stimulus epochs, and narrowband increase was seen in the low frequency for house and face-triggered epochs compared to inter-stimulus epochs.

1.1.7. Feedforward/Feedback processing

Feedforward processing in the brain refers to the input signal propagating from early sensory brain region to higher-order cognitive regions. In case of vision, a feedforward processing of vision corresponds to the propagation of visual sensory input from V1 to V2, then to higher visual brain regions within the temporal lobe. The feedforward projections in the brain represent the ascending connections in the hierarchy from lower to higher-order brain regions processing the sensory information. On the other hand, feedback processing of information is the descending projections from higher-order brain regions involved in control and tuning of the lower-order brain regions in the hierarchy. Those two signals play an important and simultaneous role in different aspects of vision in the brain (Kafaligonul et al., 2015). **Figure 1.4** illustrates the interconnections between feedforward and feedback projections in the visual system in the brain (Gilbert and Li, 2013).

1.1.8. Bottom-up/Top-down signals

We use the terms bottom-up and top-down processes to refer to feedforward and feedback brain signals respectively.
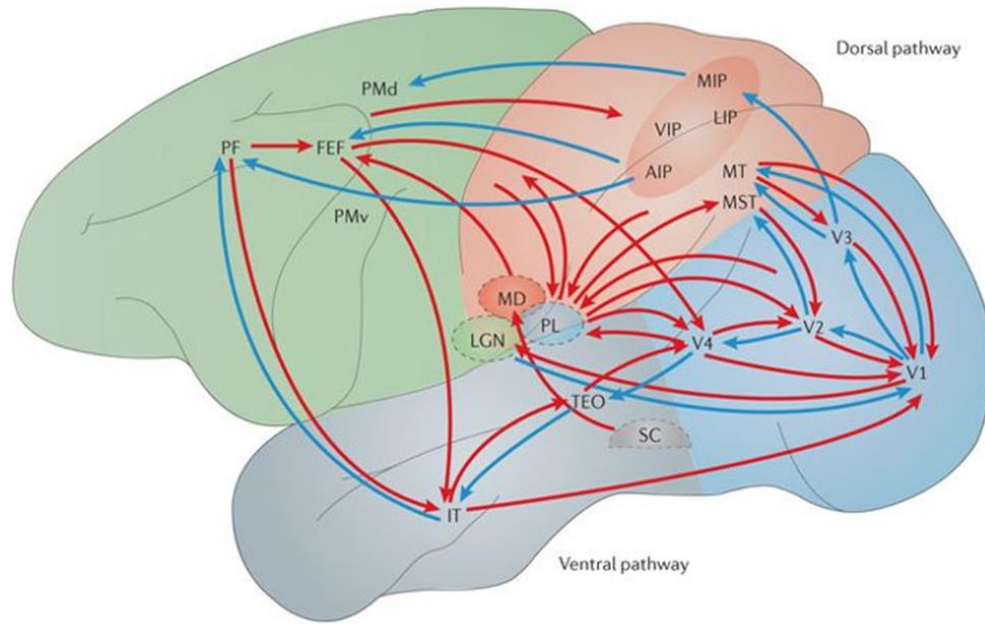
Figure 1.4. feedforward and feedback connections between brain regions in response to visual stimulus.

Adapted from (Gilbert and Li, 2013). Blue arrows represent the feedforward connections between brain regions in response to a visual stimulus, and the red arrows represent the feedback connections from higher order visual areas to lower order visual areas in the visual hierarchy. Feedback connections are present for every feedforward connection. AIP: anterior intraparietal, IT: inferior temporal, LIP: lateral intraparietal, MIP: medial intraparietal, MST: medial superior temporal, MT: medial temporal, PMd: dorsal premotor, PMv: ventral premotor, TeO: tectum opticum.

1.2. The visual perception system

1.2.1. General overview

Visual information presented to the eye is relayed to the brain from the retina via the lateral geniculate nucleus of the thalamus to the primary visual cortex (V1) in the occipital lobe. Our understanding of the primary processing of visual information as it is presented to the brain comes from early studies in cats showing that V1 is the host of neurons representing distinct specific receptive fields, which correspond to a particular region within the visual field that are sensitive to orientation and direction of light (Hubel and Wiesel, 1959, 1961, 1962). Subsequent studies investigating visual processing beyond the primary visual cortex have demonstrated that going from primary visual cortex to higher-order cognitive areas is associated with increase of the size of receptive fields and decrease of sensitivity to specific spatial features of the seen object. These changes in the response properties that take place along the visual processing of images are associated with loss of sensitivity to spatial location and spatial features of the image and increase in the ability to recognize an object as a whole (Desimone et al., 1984).

Visual processing in the brain takes place in two different yet arguably interacting streams: the dorsal stream or the "where pathway" that processes the spatial location of the object in space, and the ventral stream or the "what pathway" that processes the identification and recognition of the visual object (Goodale and Milner, 1992). In the work presented in this dissertation, I focused on studying higher-order visual processing in the brain that underlines the recognition and categorization of visualized objects independent of their location in space. Although object categorization have been predominantly studied in the temporal lobes using imaging and electrophysiological studies, it is anticipated that

object recognition and selectivity is not limited to the temporal lobe (Joseph, 2001). In the following sections, I review prior work on object recognition in different regions of the human brain.

1.2.2. Object selectivity in the temporal lobe

Recognition of specific object categories in the brain was first investigated during awake craniotomies by Wilder Penfield (Penfield and Perot, 1963). Penfield reported that when he stimulated the fusiform and parahippocampal gyri, patients experienced hallucinations of faces and places respectively (Penfield and Perot, 1963). When functional brain imaging and advanced electrophysiological tools became available, these two category-specific brain regions were further studied and confirmed in the human brain using functional Magnetic Resonance Imaging (fMRI) (Joseph, 2001), local field potential (LFP) recordings (Allison et al., 1999), and single unit recordings (Kreiman et al., 2000b). Supporting these finds were earlier studies on patients with brain lesions reporting the loss of ability to recognize faces in patients with lesions to the fusiform gyrus (Damasio et al., 1982), a condition known as prosopagnosia. Yet, patients with lesions to the fusiform gyrus retained the ability to describe some of the features of the seen faces. Place selectivity has been consistently reported in the PPA within the ventral temporal lobe, located medial to the face-selective region, the fusiform face area (FFA) (Joseph, 2001). Although faces and places were the most commonly studied object categories, further studies using fMRI showed the ability of the temporal lobe to discriminate among many object categories (Chao et al., 1999), and single neuron recordings showed the ability of single neurons to decode for multiple categories (Kreiman et al., 2000b). Decoding of object categories was

23

also reported human medial temporal lobe using local field potential and single neurons recordings (Kreiman et al., 2000b; Kraskov et al., 2007).

1.2.3. Object selectivity extends beyond temporal lobe

Even though category-based object recognition was extensively reported within the temporal lobe using different neuroimaging and electrophysiology techniques, object selectivity is rather broadly distributed in the brain. Using intracranial EEG recordings from patients confronted with different visual object categories, Vidal et al. showed that despite the prominent existence of electrodes encoding for different object categories in the temporal lobe, the frontal and occipital lobes were also involved in encoding visual categories (Vidal et al., 2010). Moreover, a meta-analysis of 14 fMRI studies conducted on category-specificity responses in the human brain showed a broad distribution of object selectivity regions (Joseph, 2001) (**Figure 1.5**). The same report also confirmed the reported distribution of face selectivity regions lateral to manufactured objects and natural scene selectivity regions within the medial temporal lobe (**Figure 1.5**).
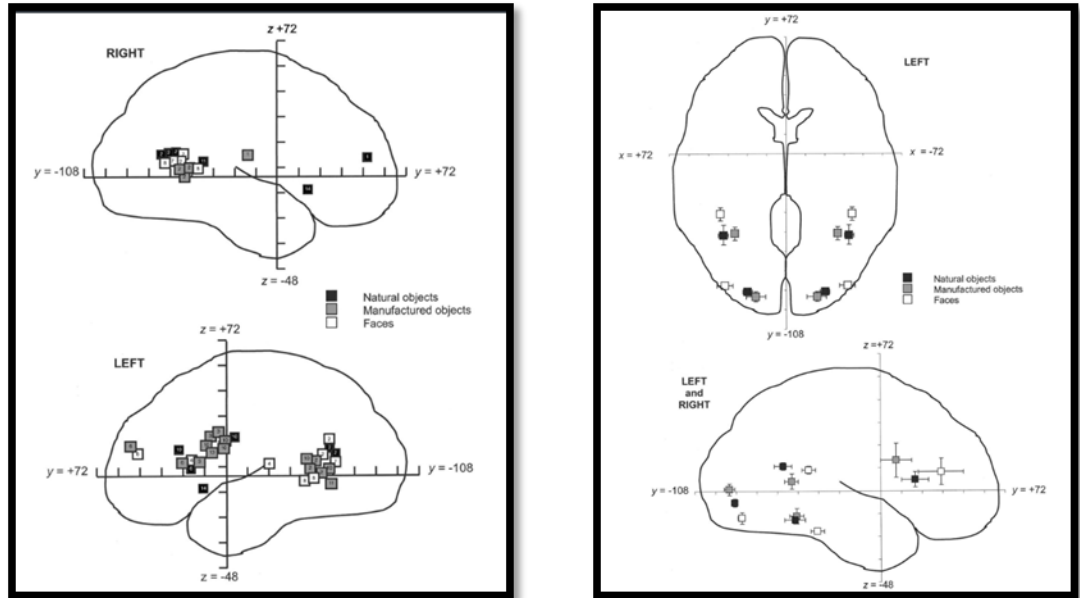
Figure 1.5. Meta-analysis of reported distribution of object based category in human brain.

Modified from Joseph et al (Joseph, 2001). Left panel: sagittal view showing brain loci reported, in published fMRI reports, to be involved in the recognition of natural objects (black squares), manufactured objects (gray squares), and faces (white square). Right panel: axial and sagittal views showing the mean and standard error bars of activation in brain loci in response to the same object categories presented in the left panel.

Interestingly, subcortical regions were also reported to be involved in visual processing and object-based selectivity in the brain. Specifically, the caudate and putamen within the neostriatum showed object-category sensitive response, a finding that is not unanticipated given the presence of dense inputs to the striatum from the temporal visual regions (Yeterian and Van Hoesen, 1978). These findings were later confirmed by studies on single neurons in non-human primates showing both visually-responsive neurons and object-category selective neurons in the caudate and putamen (Yamamoto et al., 2012; Kunimatsu et al., 2019). More specifically, the tail region of caudate and putamen, which is in close proximity to the temporal lobe, was found to control saccade and attention among objects based on their historical value to guide subsequent behavior involving movement to reach to the object (Yamamoto et al., 2012; Kunimatsu et al., 2019).

1.2.4. Significance of a broadly distributed visual representation system

The broad distribution of visual information in the human brain is expected given the need for visual inputs to guide motivational, emotional, motor and cognitive outputs of cortical and subcortical areas (Kourtzi and Connor, 2011). For instance, the medial temporal lobe is implicated in memorization of visual information, the prefrontal cortex is key in rule-based tasks including those based on visual sensory information, and the basal ganglia requires visual information and feedback for tuning movements in response to salient visual objects (Kourtzi and Connor, 2011). Thus, object selectivity in brain regions involved in visual category learning is not surprising. Even though some brain regions are not essential for object recognition, like the prefrontal cortex for example, the visual object selectivity of those areas allow for optimizing relevant behavior, in the case of the

26

prefrontal cortex it helps in directing attention to the targeted object category (Duncan, 2001; Ashby and Maddox, 2005).

1.2.5. Temporal propagation of unconscious and conscious visual information

Visual inputs propagate from the primary visual cortex V1 to higher-order cognitive regions in the brain. Latency of electrodes' response to visual stimuli within the studied brain region increases along the hierarchy of visual processing. This response latency has been previously studied in the macaque visual system (Schmolesky et al., 1998) as shown in **Figure 1.6**.

Time from Stimulus onset (msec)
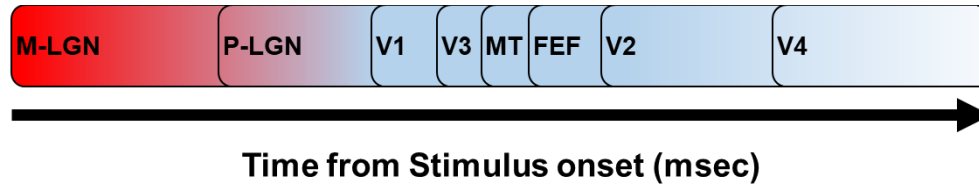
Figure 1.6. The order of latency to respond of different brain regions involved in early visual processing of a visual stimuli in macaque.

M-LGN: magnocellular layers of the lateral geniculate nuclei, P-LGN: parvocellular layers of the lateral geniculate nucleus, V1, V2, V3, V4: cortical visual areas, MT: middle temporal area, FEF: frontal eye field.

Even though the response delay in the visual system of the macaque may be quantitatively different than that of man, the same order in delay still applies (Gomez Gonzalez et al., 1994; VanRullen and Thorpe, 2001). A magnetoencephalography (MEG) study showed that a chromatic grating, encoded beyond V1, would evoke a stable response in the striate cortex with a peak around 100-140 msec (Fylan et al., 1997), compared to the 60-80 ms delay observed in V1 }(VanRullen and Thorpe, 2001).

Interestingly, in an human intracranial EEG study using images displayed to subjects between 16 msec and 66 msec, the average evoked and gamma power response to faces did not change whether the subjects recognized the images (conscious vision) or not (unconscious vision)(Fisch et al., 2009). The concept is that electrodes within the occipito-temporal cortex respond to the stimulus in the visual field regardless of visual awareness of the object of the response. The response in the occipito-temporal cortex started at 150-200 msec and outlasted the time of image display. This delayed response to object recognition in the temporal lobe was also observed on MEG studies showing that face categorization response is triggered around 100 msec (M100) in the ventral temporal lobe (Liu et al., 2002), even though face identification is correlated with a later component at 170 msec (M170). Thus, object recognition is a delayed cerebral response compare to vision consistent with the processing hierarchy where object categorization occurs in higher-order cortical regions.

Going higher in the visual hierarchy, the medial temporal lobe was reported to have a further delayed response (369±53 msec) when subjects were exposed to nine object categories (including faces, cars, and spatial layouts) during LFP recording

(Kreiman et al., 2000b). The stimuli were presented for 1000 msec, and the duration of the response ranged from 53 to 1190 msec. On the other hand, fronto-parietal cortex implicated in perceptual awareness was reported to have a delayed response of more than 300 msec after stimulus onset (Del Cul et al., 2007; Gaillard et al., 2009).

Understanding the time dynamics of different regional cortical response to visual information is key to design the appropriate experiments aiming at understanding visual processing in the brain when including higher-order cortical processing centers. This temporal pattern of responses is also critical for the selection of the appropriate size of time windows used in subsequent analyses.

1.2.6. Synchronous and asynchronous aspects of neuronal activity

Following confrontation with a visual stimulus, changes observed at the level of the LFP recordings are reflective of changes at the level of the neuronal population around the recording site. Those changes are of two types; modulation of individual neuronal activity in a synchronous manner (rhythmic) leading to oscillatory behavior, or in an asynchronous manner. The latter type results in a broadband increase (non-rhythmic) in the power of the spectral density across a wide range of frequencies (1-200Hz). This concept, simulated by Miller and his colleagues (Miller et al., 2009a) and illustrated (Miller, 2015) in **Figure 1.7**, is key to understand the power modulation reflected in the LFP after stimulus onset. As Miller explained (Miller, 2015), asynchronous synaptic input would manifest, at the level of LFPs, as a speeding up of a random walk that is hard to notice unless taken to the frequency domain where it would be clearly emphasized as a broadband spectral increase, and it reflects local cortical activity. Whereas synchronous neuronal activity is easily depicted in the recording and would be reflected by a narrowband spectral peak. The

emerging synchronous activity (rhythm) could be the result of a feedback loop involving subcortical cortices like the cortico-striato-thalamic loop, and the state of the components would determine if they get in synch or out of synch. Synchronization results in an increase the narrowband peak whereas desynchronization results in a decrease in this peak. Alternatively, another source of synchronization could be a feedforward process, an example of which is the visual input propagating from the thalamus to V1 as a result of a time-locked response triggered by special features. This visual stimulus would first activate the pyramidal cells then synchronize lateral inhibition to create an oscillatory pattern (Miller, 2015). Using this concept, we can better understand the previously reported modulations in the spectral power upon visual processing in the brain as explained in the next section.
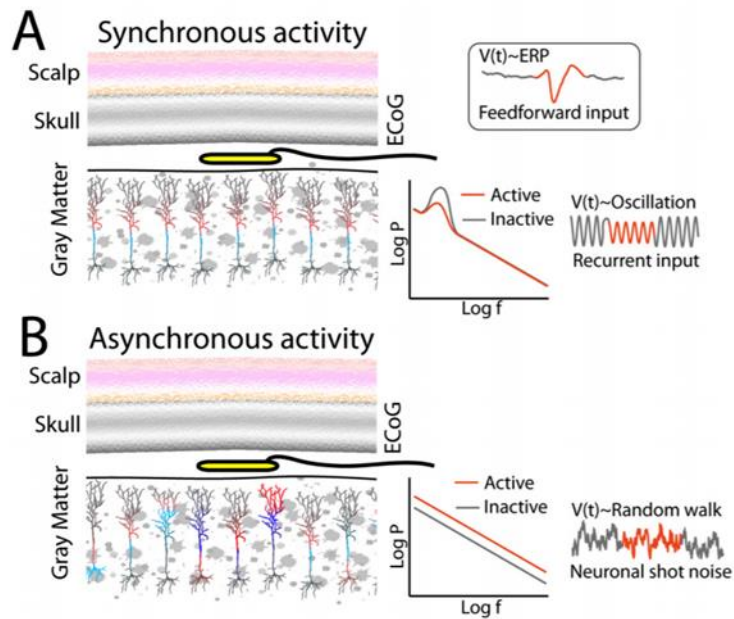
Figure 1.7: The concept of synchronous vs asynchronous activity as illustrated in (Miller, 2015).

The figure describes the effects of synchronous vs. asynchronous neuronal activity on the spectral domain patterns and ECoG raw signals as simulated by Miller et al. (**A**) Synchronous activity shows as a narrowband peak in the spectral domain, and a corresponding oscillation in the recorded ECoG signal. (**B**) Asynchronous activity is seen as a broadband modulation in the spectral domain and as a corresponding increase in the velocity of the random walk in the recorded ECoG signal.

1.2.7. Spectral modulation during visual processing

1.2.7.1. The Famous Gamma

A commonly reported robust and narrowly confined gamma oscillation (40-60 Hz) has been proposed as the key element in visual encoding in the visual cortex (Tallon-Baudry et al., 1997; Hoogenboom et al., 2006; Fries et al., 2008; Brunet et al., 2014). However, more recent studies have questioned the functional primacy of the narrowband gamma responses in vision (Ray and Maunsell, 2010; Jia et al., 2013; Hermes et al., 2015). Hermes et al. (Hermes et al., 2015) showed that a narrowband gamma response can be induced by stimuli with specific size, contrast, textures, and patterns. However, no evidence of a consistent narrowband gamma response was reported for many recording sites in the fusiform or parahippocampal gyri when seeing a face or a building respectively, even though both areas have been consistently implicated in the perception of these categories of visual stimuli. Rather, the authors noted stimulus-evoked power variations over a wide range of frequencies - termed a "broadband response"- in these higher-order cortical regions (Hermes et al., 2015). In another human LFP study, power variation across the entire range of gamma frequencies within the ventral temporal cortex, rather than a narrowband gamma, was reported to be selective for the presented object categories (Miller et al., 2014; Miller et al., 2016).

Moreover, to explain the previous reported power increase over a wide range within the gamma band (Jacobs and Kahana, 2009; Vidal et al., 2010), Miller and his colleagues (Miller et al., 2014) argued that what seems to be a gamma band modulation is actually a broadband modulation across all the frequency bands that is masked by the low frequency modulations. Using principal component analysis (PCA) they successfully decoupled the

spectral power of the rhythmic synchronous narrowband activity in the brain from non-rhythmic broadband asynchronous activity in multiple modalities including motor and visual tasks. This was basically done by reconstructing the power spectral response of the rhythmic part using principal components 2,3, and 4, and reconstructing the power spectral response of the non-rhythmic part using all other principle components (mainly the first principal component) not used in the reconstruction of the rhythmic part.

1.2.7.2. The neglected other frequencies

Even though low frequency oscillations were reported to be modulated during visual processing in the brain, they are usually skipped from the analysis. An example from our data is shown in **Figure 1.8** after a visual stimulus is presented for 500 msec. The variation along the low frequency bands in addition to the broadband gamma increase in power can be easily appreciated.
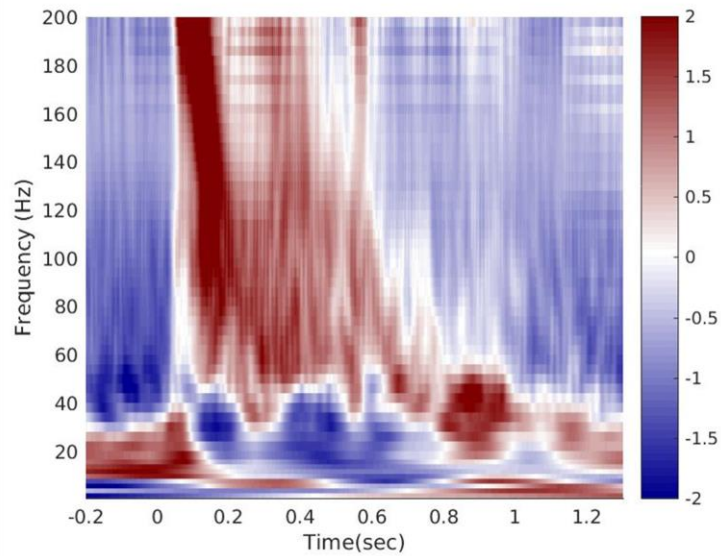
Figure 1.8: Spectrogram of LFP response from a recording site in the visual cortex of a subject confronted with visual stimuli.

The figure shows a spectrogram of z-scored power modulation across time and frequency (1-200 Hz) showing the average response of a recording site within the visual cortex (calcarine) to 450 images displayed on the screen for 0.5 sec, and followed by ISI for 1 sec. The recording site responds instantly after the onset of stimuli (presented at time 0 sec), with a clear decrease in low frequency alpha-beta range, and a broadband increase for when the image is on the screen.

Low frequency alpha-beta power modulation (decrease) is reported to be important to facilitate vision in the occipital lobe (Pfurtscheller et al., 1994; Pfurtscheller and Lopes da Silva, 1999). At rest, i.e. in the absence of visual stimuli, a high-power alpha rhythm is noticed, and after the onset of a visual stimuli the power of alpha decreases. This decrease is referred to as the desynchronization of the cortico-thalamic loop to allow for visual encoding in the brain (Miller et al., 2010b). On the other hand, an increase in the power of theta in the hippocampus is thought to be important to facilitate encoding of long-term memory in the hippocampus. It is possible that because the delta to beta bands represent relatively slow signals in the brain (as opposed to gamma), those bands were dropped from the analysis of object category-based encoding in the brain and were specifically reported in top-down feedback cognitive processing studies like attention, memory, and decision making. However, in these cognitive functions performed at higher-order region, the seen object needs to be recognized, categorized or contextualized to generate the corresponding response or behavior.

After a thorough review of the literature on visual category-based decoding using low frequency aspect of LFP recordings, we found that only few studies have investigated and eventually implicated the low frequency bands in visual categorization in the brain. An overview of these studies is presented here:

- Vidal and his colleagues (Vidal et al., 2010) showed that alpha-beta band decodes seven visual categories across widely distributed recording sites across the human brain.

- Majima and his colleagues (Majima et al., 2014) showed that delta – theta bands (1-10Hz) have the highest decoding accuracy compared to the other bands when

decoding visual object categories. They also showed that decoding at this range is robust and immune to changes with shuffling of the seen images unlike the other bands that show changes in responses with shuffling.

- Miller and his colleagues (Miller et al., 2014) showed that the main spectral components that vary across stimuli of buildings, faces, and interstimulus interval (ISI), consist of a broadband pattern, and narrowband pattern at the theta band. Even though when power variation across frequencies was studied using principal component analysis, it was evident that the second and third principal components contained a robust low frequency component. Although this low frequency component was reported, it was not studied to compare its decoding accuracy to that of the broadband effect studied by this group.

- Bastos and his colleagues (Bastos et al., 2015) reported the involvement of reported theta oscillation (3-4 Hz), which actually includes delta oscillation too, as a feedforward signal during visual attention task in macaques.

- Isik and his colleagues (Isik et al., 2018) recently showed the ability to decode using single trials in a movie the onset and the actual scene at which an abrupt change takes place. They only studied the alpha band (8-15Hz) among the low frequency bandsto show the ability of low frequency bands to decode such information.

- Davidesco and his colleagues (Davidesco et al., 2013) showed an increase in broadband gamma after the onset of visual stimuli. Even though both delta and other low frequency modulation were present in the spectrograms after the onset of visual stimuli, these bands were dropped from the analysis without a clear rationale.

- The role of delta oscillations has been reviewed by Harmony (Harmony, 2013) reporting a number of cognitive functions where delta band oscillations were implicated such as attention and detection of motivationally salient stimuli.

1.2.8. Selectivity of spectral patterns to object categories

An important studied aspect of spectral encoding of broadband and narrowband low frequency is the selectivity index of each pattern to specific object categories. The selectivity index is a metric that studies how selective is the response of one spectral pattern to a specific stimuli category versus another, and how sparse is the representation of one spectral pattern compared to another. The significance of this metric, despite being measured differently across studies, is that it gives an insight into the type of information encoded by different spectral patterns. A sparse representation or high selectivity index would mean that the studied spectral pattern is sharply tuned to a specific stimulus, whereas a low selectivity index indicates that the studied spectral pattern is not selective to a specific stimulus. Both studies by Vidal et al. (Vidal et al., 2010) and by Miller et al. (Miller et al., 2009b) showed that broadband activity has high selectivity indices whereas narrowband low frequency showed low selectivity index.

1.2.9. Spatial distribution of spectral patterns

The broadband patterns with high selectivity indices were shown to be more focused in selective brain regions (Miller et al., 2014). For example, a broadband pattern was reported to be highly selective to faces and places in FFA and PPA respectively (Miller et

al., 2016), and in brain regions corresponding to tongue and finger movements in the motor area (Miller et al., 2010a). On the other hand, low frequency narrowband patterns were more distributed within and around the brain regions selective for the specific studied visual or motor stimuli (Miller et al., 2009b; Miller et al., 2010a).

1.2.10. Spectral patterns relation to BOLD and single neurons firing rate

In an effort to integrate the knowledge across different functional investigation techniques to understand how the brain processes visual information, it was shown that modulation in the power of the broadband pattern of the LFP recordings correlates best with an increase in single neuronal firing rate (Manning et al., 2009) and with increase in fMRI BOLD signal (Hermes et al., 2017). Low frequency narrowband pattern could be positively or inversely correlated with the rate of single neuronal firing or BOLD signal depending on the direction of change in power at the low frequency narrowband. Integrating information from different brain recording and imaging techniques allows improves our understanding of the cognitive processing in the brain to reach an understanding in terms of several levels of description and the relations across them.

1.3. Top-down modulation of vision

We have this far discussed prior work that investigated vision as a sensory input to the visual cortex that propagates to higher-order brain regions. However, passive viewing of images/videos doesn't represent the complexity of the everyday life scenarios where vision is almost always oriented to a specific object in the space or affected by the

behavioral task that the person is performing. This cognitive influence on how we perceive the sensory input is what we refer to as top-down modulation of vision, or feedback processing in the brain. Attention is one of the obvious examples of top-down controls in the brain that has been shown to modulate visual perception when studied at the level of BOLD changes on fMRI (Andersson et al., 2011; Cukur et al., 2013), LFPs on ECoG (Ramot et al., 2012), and single neuron recordings (Fries et al., 2001). Mental imagery is yet another example of top-down signals that interact with the visual system. During mental imagery, an image is generated in the brain by a sole top-down effect in the absence of a visual sensory input.

1.3.1. Feedforward and feedback connections target different layers in the visual cortex

Feedback and feedforward projections have been shown to be distinct at the level of cortical microarchitecture. The granular layer (layer IV) receives feedforward projections (Felleman and Van Essen, 1991) that originate from the supragranular layers (Markov et al., 2014). These projections are reported to have gramma band synchrony (Buffalo et al., 2011). On the other hand, feedback projections avoid the granular layer (Felleman and Van Essen, 1991), and originate from the infragranular layers (Markov et al., 2014) with a predominant alpha-beta band synchrony (Buffalo et al., 2011; Xing et al., 2012).

1.3.2. Visual attention

An unanswered question about the encoding of visual information in LFP spectra is the influence of visual attention. It is known that attention can modulate the action potential firing rates (Moran and Desimone, 1985; Fries et al., 2001) and blood-oxygen-level-dependent (BOLD) signals (Cukur et al., 2013) during the perception of visual stimuli. However, there is some evidence that, at the LFPs, the encoding of information about what is attended and what is seen may be differentially distributed across the frequency spectrum (Bastos et al., 2015; Jensen et al., 2015; Michalareas et al., 2016). Indeed, there is cumulative evidence that top-down (e.g., visual attention) signals are generally encoded at lower frequency bands (<30Hz ranging from δ (1-4Hz) to β (14-30Hz)) in the sub-gamma range of the frequency spectrum (Klimesch, 1999; Klimesch et al., 2011; Jensen et al., 2015; Michalareas et al., 2016; Helfrich et al., 2017). Thus, the frequency bands most relevant to the encoding of visual information may depend strongly on how attention varies during viewing.

In this work, we study which frequency bands are relevant to encoding natural scenes during sustained attention to a specific object category by analyzing LFP recordings from epileptic patients. We address key questions related to spectral encoding in this context, namely: Which frequency bands are subject to the most power variation upon varying the category of attended and/or seen objects? And can attention and vision be separated at the spectral level?

1.3.2.1. Spectral modulations during visual attention

1.3.2.1.1. The Famous Alpha

Visual attention as a feedback cognitive function in the brain was mainly reported over the low frequency range. In the visual cortex, a decrease in the power of alpha band oscillations was the most commonly reported modulation taking place during visual attention (Pfurtscheller et al., 1994; Thut et al., 2006; Klimesch et al., 2011). This decrease was also shown, using magnetoencephalographic (MEG), to be lateralized to the location and spatial distribution of the attended object in the visual field (Ikkai et al., 2016).

1.3.2.1.2. The other frequencies

Albeit the extensive reporting of alpha oscillation in the visual cortex during visual attention tasks, other oscillations ranging from delta to beta were also reported to be involved in top-down attention (Klimesch, 1999; Klimesch et al., 2011; Jensen et al., 2015; Michalareas et al., 2016; Helfrich et al., 2017). We will refer to attention here as "top-down attention" since an alternate bottom-up attention effect has been described as a response to salient stimuli and has been shown to be encoded by high gamma oscillations (Bastos et al., 2015).

1.3.2.2. Spatial distribution of category-based visual attention

In a pioneer fMRI study (Cukur et al., 2013), Cukur and his colleagues showed the effect of category based visual attention on shifting human's brain response to the attended category over a widely distributed brain network during observation of a movie scene. The effect of attended visual category of modulating the response to seen frames was present even in the absence of the attended category from the studied movie scene. This study was

one of few whole brain studies that addressed category based visual attention where the subjects watch a movie containing a wide range of object categories. Previous studies showed the effect of tuning in selective brain regions on BOLD signal (O'Craven et al., 1999; Peelen et al., 2009), and on the response of single neurons within the early visual cortex (David et al., 2008) and in the pre-frontal cortex (Warden and Miller, 2010). A yet unexplored area of investigation is the spectral effect of attention on category-based visual attention in human brain. This investigation cannot be performed using fMRI studies that lack the ability to test the spectral variation occurring during attention. Single neuron recording studies didn't address the ability of neurons within a studied brain region to encode for different categories during the category-based attention.

In the work presented here, we addressed category-based visual attention using LFP recordings to study the spectral domains and determine which frequency patterns are involved in vision and/or attention, and to study the ability of those spectral pattern to decode different combinations of seen or attended categories.

1.3.3. Mental imagery

Top-down processes in the brain include a wide range of cognitive functions, and mental imagery is one of the best manifestations of outputs from the top-down system (Kosslyn et al., 2001). Visual imagination highly overlaps with visual perception, with the difference of lack of sensory input to the brain in case of mental imagery. Despite the presence of evidence from fMRI regarding the overlap between perception and mental imagery (Kanwisher et al., 1997; Bartolomeo, 2008), this overlap may not be complete. Evidence from patients with isolated deficits in one of the two domains provide preliminary evidence that lesions in the left temporal lobe affects mental imagery with preservation of

visual perception, whereas lesions within the occipital lobe may affect perception while mental imagery is intact (Farah, 1988). It has been also proposed that mental imagery ability is modality-specific (Fallgatter et al., 1997; Schifferstein, 2009) based on lesion studies showing isolated loss of visual mental imagery while mental motor, auditory, olfactory, and gustatory imagery are preserved (Bartolomeo et al., 2013). In order to better understand the connection between mental imagery being modality-specific and its preservation in cases where vision itself is damaged, Kreiman and his colleagues (Kreiman et al., 2000a) studied single neurons within the medial temporal lobe of human brain using LFP and showed that a subset of neurons were exclusively responsive to mental imagery as opposed to vision itself. It is not surprising that mental imagery shares neuronal substrates with working memory since during mental imagery the subject retain the imagined picture in the brain while sustaining attention to that picture for successful imagination (Albers et al., 2013). Mental imagery and its retention in the brain requires a wide repertoire of cognitive control that humans apply as part of the learning process leading to their survival and improvement of functional ability. Moreover, based on neuroimaging experiments, mental imagery uses a large network of top down cognitive processing that involves frontal, parietal and temporal lobes (Ishai et al., 2000; Ganis et al., 2004).

1.3.3.1. Visual mental imagery

Visual perception and mental imagery in the human brain were studied using fMRI (Kanwisher et al., 1997; Bartolomeo, 2008) and single neurons recordings (Kreiman et al., 2000a) with consistent overlap in observations from both modalities. However, studies in patients with damage to the visual circuitry provided better insight into the close correlation

44

between the processing of imagined and visualized objects. Interestingly, damages to a specific track affecting one aspect of vision in patients also affected the same aspect in mental imagery (Levine et al., 1985). To illustrate, damage to the ventral stream affecting the recognition of faces also affected the ability to imagine faces, whereas damage to dorsal stream affecting the ability to locate objects in space also affected the mental imagery of spatial recognition such as indicating when the eyes are closed the spatial location of furniture in a room (Levine et al., 1985). Along the same line, brain injury involving impaired visual recognition of colors also impaired the mental imagery of the corresponding colors too (De Vreese, 1991). Single neurons recordings in the medial temporal lobe showed a high percentage of neurons whose activity is shared by vision and mental imagery, but still an independent subset of neurons were only responsive for either vision or mental imagery (Kreiman et al., 2000a). This latter finding would likely explain what Farah and his colleagues reported in a series of clinical cases where patients with lesions resulting in the impaired ability to see but not to imagine or vice versa (Farah, 1984).

1.3.3.2. On the difference among mental imagery, attention, and working memory

One of the major debates in the field of mental imagery is the interaction with other cognitive processes like working memory and attention, since having a mental imagery during a task that involves attention to visual stimuli may also fit the definition of working memory (Albers et al., 2013). Mental images may also be created by modifying a memory or by simple generation of new object in mind and requires sustained attention to maintain a vivid imagination of the object. In a recent review, Pearson et al. (Pearson et al., 2015)

discussed how people with high ability to perform mental imagery utilize it in visual working memory tasks, whereas people with poor mental imagery would rely on non-visual strategies to perform a visual working memory task. Thus, mental imagery is not required for all visual working memory tasks.

1.3.3.3. Spectral distribution of mental imagery

Little is known about the spectral distribution of mental imagery, mainly because of the disconnect between research on working memory and mental imagery. Still, it has been demonstrated that motor mental imagery exhibits a similar decrease in beta oscillation and increase in gamma band to that seen in actual movement as compared to rest (Miller et al., 2010a). On the other hand, when studied in the context of working memory, van Gerven and his colleagues studied ECoG recordings (van Gerven et al., 2013) and showed that theta/alpha band (8-14 Hz) and gamma band (65–128 Hz) modulations are associated with the stimuli-specific neuronal activity in different recording sites within the temporal lobe.

1.3.3.4. Studying the visual mental state

In part of this work, we study the response of the brain to different visual mental states in order to better understand visual mental imagery encoding. We designed an experiment that allows the comparison of the brain response to passive viewing of images, ISI gray screen, active looking at images to memorize them, and mental imagery of the memorized images. We used the same approach we applied to category-based visual attention **(Chapter 2)** to reveal the pattern of neuronal activity involved in different visual mental states. We anticipate that mental imagery follows the spectral patterns characteristics of a top-down process. This top-down process uses recall and maintenance of image in the working memory during the actual imagination of an image, and is

46

anticipated correlate with a low frequency component likely related to the top-down effect in the brain and a high gamma component to vividly recall the image and maintain it in memory during recall.

1.4. The rationale and aims of the dissertation

1.4.1. Rationale and hypothesis

Cerebral processing of external stimuli is characterized by an intricate circuit of top-down and bottom-up processes, also referred to as feedback and feedforward processes respectively. Bottom-up processes involve external sensory information whereas top-down processes involve cognitive activities initiated within the brain. Top-down and bottom-up signals often co-exist in a spiral processing paradigm that may be difficult to disentangle and form a substrate for physiological processes such as conscious awareness or mental imagery, and pathological perceptual events such as illusions or neglect. Since top-down and bottom-up processes represent distinct cerebral activities, they are expected to have different underlying circuitry characteristics. Neuronal activity recorded from the brain is rich in various components including phase, amplitude, and frequency bands that may mediate different aspects of neuronal encoding. Decomposing the signal into its frequency components would show the power at different frequency bands. This is known as spectral distribution of the signal which has been shown to reflect different communication pathways. In order to identify how the brain encodes top-down and bottom-up processes, it is key to investigate their corresponding spatial distribution and spectral distribution. Whereas spatial distribution provide insight into the neuroanatomical substrates of top-down and bottom-up for a given stimulus, spectral distribution identifies the circuit-level interaction patterns within or across these substrates. Therefore, techniques that directly

records high temporal resolution brain activity, such as LFP recordings, are suited to address questions about spectral distribution. This work aims to investigate the spatial and spectral distribution of top-down and bottom-up processing using LFP recordings. We will approach top-down processing by studying visual attention and mental imagery, and bottom-up processing by studying perception of photographs.

Visual sensory inputs are propagated in a feedforward manner from the retina to the primary visual cortex V1. Further processing in the visual system occurs in an integrative way where small receptive fields converge into bigger fields as signal propagates to higher-order cognitive areas until the image is abstractly perceived. During top-down processing, information descends from abstract regions to lower levels, expectedly through differential diffusive tracts as opposite to bottom-up processing. Spatially, bottom-up circuits are expected to converge into focal regions while top-down circuits follow a divergent trajectory. Simulation of neuronal models showed that asynchronous increase in activity of single neurons result in a broadband spectral pattern characterized by an increase of power over a wide range of frequencies. Synchronous activity of a neuronal population at a given frequency results in a narrowband spectral pattern characterized by a peak in the spectrogram at that specific frequency. Therefore, investigating visual encoding given the new understanding of the relation between the spectral distribution and the underlying neuronal activity would provide novel insight on top-down and bottom-up loops. This work will benefit from the characteristics of LFPs to test the central hypothesis that top-down and bottom-up processes exhibit an asymmetric spatial and spectral distribution; where top-down activity is spatially diffused and spectrally confined whereas bottom-up activity is spatially confined and spectrally diffused over a broadband range. We will use LFP

recordings from epileptic subjects to study using visual processing in the human cortical areas as a model. The interest of this work is bi-dimensional: spatial and spectral. The spatial dimension investigates visual encoding over a wide range of cortical regions, and the spectral dimension studies the pattern of power spectral density over a broad spectrum (1-100Hz).

1.4.2. Dissertation aims

The specific aims for this dissertation will be covered in independent chapters and are listed here:

- **Specific aim 1 develops a computational approach to identify the spatial and spectral distribution of perceptual and attentional encoding of categorized visual stimuli in the human brain using LFP data.** As discussed in our introduction, we anticipate that visual perception encoding representing bottom-up processing is spectrally diffuse over a broadband range of frequencies, and spatially confined to the temporal lobe. However, visual attention encoding representing top-down processing is expected to be spectrally limited to a narrow band frequency range and spatially diffuse in the brain. In this aim, we intend to build spectral encoding models using broadband and narrowband spectrograms and to apply them to different combinations of seen and attended stimuli to disentangle the two components of visual object processing (attention and vision). **(Chapter 2)**

- **Specific aim 2 investigates the spatial and spectral distribution of mental imagery in the human brain**. Since mental imagery is a top-down activity that that exhibits significant spatial overlap with vision, we predict that it will be spatially broad across diffuse brain regions. Yet, since mental imagery includes the

maintenance of images reverberating in the brain while engaging in imagination, we expect encoding of mental imagery to spectrally involve the gamma band along with the low frequency bands corresponding to the top-down effect of attention in the brain. We intend to test this aim by applying the same spectral encoding model used in specific aim 1 to different visual mental states that involve passive viewing of images, ISI gray screen, active viewing of images to memorize them, and mental imagery of the memorized images. We believe that top down and bottom-up processing are distinguished at the circuit level, but currently one can only speculate what these circuit differences might be. Successful completion of these aims will uncover the spectral distinction of these signals. Such information will lead to a better understanding of circuitry underlying top-down and bottom-up processes and would give potential explanations of brain pathologies such as dementia, autism, or attentional deficit disorders at the level of neuronal circuitries. Finally, understanding the mechanisms involved in encoding visual information will provide valuable information for the design of brain computer interfaces to favorably alter neuronal encoding to ameliorate disease-related deficits. **(Chapter 3)**

CHAPTER TWO

VISUAL ATTENTION

2.1. Introduction

A longstanding challenge in systems neuroscience is to understand how variations in sensory and cognitive states are encoded in variations in the power spectrum of local field potentials. During sensory and cognitive experiments the frequencies at which variations in power are most tightly coupled to variations in experimental conditions depends heavily upon the brain area under study and the variables manipulated in the experiment. Thus, the first step in many local field potential (LFP) studies of sensory or cognitive processing is to identify the most appropriate frequency bands to examine for relationships to the stimulus or task.

In visual neuroscience, questions about the encoding of visual stimuli are often addressed by examining frequencies above 30Hz exclusively—the so-called "gamma" range. There is ample prior work to justify why the gamma band is the default frequency range of interest. For example, many studies have reported a robust and narrowly confined (40-60Hz) increase in power in the gamma range in response to artificial and natural scenes (Fries et al., 2001; Fries et al., 2008; Fries, 2009; Brunet et al., 2014). It has been argued that this so-called "narrowband-γ" is in fact required for the perception of both objects and natural scenes via the visual cortex (Tallon-Baudry et al., 1997; Hoogenboom et al., 2006; Fries et al., 2008; Brunet et al., 2014).

Recent studies have questioned the functional primacy of narrowband gamma responses in vision (Ray and Maunsell, 2010; Jia et al., 2013; Hermes et al., 2015). For example, Hermes et al. (Hermes et al., 2015) showed that while a robust narrowband gamma is indeed be induced by some types of visual stimuli, a narrowband gamma response in response to pictures of faces or buildings was largely absent for recording

sites in the fusiform or parahippocampal gyri, even though both areas have been heavily implicated in the perception of these categories of visual stimuli (Kanwisher et al., 1997; Chao et al., 1999; Haxby et al., 2001). Rather, these authors noted stimulus-evoked power variations over a wide range of frequencies--termed a "broadband response"--in these high-level visual areas. In another human electrocorticography (ECoG) study, power variation across the entire studied range of gamma frequencies (30-200 Hz)--in contrast to a narrowband gamma response--within the ventral temporal cortex was reported to be selective for the presented object categories (Miller et al., 2014; Miller et al., 2016). Thus, the particular spectral bands most relevant for encoding information about object category would appear to be an unsettled question whose answer is dependent on brain region and the kind of stimuli presented.

Another unsettled question about the encoding of visual information in LFP spectra relates to visual attention. It is known that attention can modulate the action potential firing rates (Moran and Desimone, 1985) and blood-oxygen-level-dependent (BOLD) signals (Cukur et al., 2013) encode information about visual stimuli. However, there is some evidence that for LFPs information about what is attended and what is seen may be encoded in different frequency bands that can in principle vary independently of one another (Bastos et al., 2015; Jensen et al., 2015; Michalareas et al., 2016). Indeed, there is accumulating evidence that top-down (e.g., visual attention) signals generally are encoded in a lower (< 30 Hz ranging from δ (1-4Hz) to β (14-30Hz), sub-gamma range of the frequency spectrum (Klimesch, 1999; Klimesch et al., 2011; Jensen et al., 2015; Michalareas et al., 2016; Helfrich et al., 2017). Thus, the frequency bands most relevant

to the encoding of visual information may depend strongly on how attention varies during viewing.

In this work, we study which frequency bands are relevant to encoding natural scenes during sustained attention to a specific object category by analyzing LFP recordings in humans. We address key questions related to spectral encoding in this context, namely: Which frequency bands are subject to the most power variation upon varying the category of attended and/or seen objects? How are information about attended and seen object categories encoded in patterns of variation in spectral power?

To address these questions, we prepared peri-stimulus power spectral density (PSD) functions for LFP signals recorded at sites on and beneath the surface of cortex, in hippocampus and amygdala. We decomposed the variation in PSDs across seen and attended stimulus categories using principal component analysis (PCA). The major PCs revealed the combinations of frequency bands that explain a substantial fraction of the variation in spectral power across different seen and attended object categories as well as across recording sites. We then analyzed variation in power along each PC at each recording site by building simple encoding models based upon seen and attended object category. When then used the encoding models to determine the spatial distribution of recording sites that encode stimulus and attentional category variation along each PC, and the sharpness of tuning along each PC. Finally, we used the encoding models to perform model-based decoding to understand how the encoding of information about seen and attended stimulus category are distributed across the frequency spectrum.

2.2. Material and Methods

2.2.1. Subjects

Eleven epileptic patients (6 males, 5 females) between 14 and 56 years old participated in the experiment. Prior to the experiment each participant underwent a surgical procedure for implantation of depth electrodes for detection of seizures within cortical and subcortical structures. The location of the implanted electrodes was determined based solely on clinical considerations. All participants provided written consent approved by the Institutional Review Board at the Medical University of South Carolina. Only one participant (S2) had an electrode grid (a transparent numbered mesh of electrodes that is placed subdurally the brain surface) over the lateral surface of the left hemisphere in addition to depth electrodes.

2.2.2. Electrode features, placement, and location mapping

The location of subdural and depth electrodes (Ad-Tech, Oak Creek, WI) varied among participants and it is listed in supplementary table 2-1. The placement of electrodes was solely guided by clinical evaluation of each participant. Each depth electrode has 10 recording sites separated along the electrode by 5mm. Each electrode has a diameter of 2.29 mm. Participant S2 had an additional grid of 8×8 recording sites with 10mm spacing between adjacent recording sites.

We used T1-weighted structural MR images taken for each post-implantation to determine the anatomical location of recording sites. First electrodes were masked in the structural images using "cost function masking" (Brett et al., 2001) in MRIcron (MRIcron, RRID:SCR_002403). Structural images for each participant were

55

then normalized to MNI space using the Clinical Toolbox (Rorden et al., 2012) within

SPM8 (SPM, RRID:SCR_007037; Clinical Toolbox for SPM, RRID:SCR_014096).

Mapping of individual recording sites on a normalized brain was visualized using

BrainNet Viewer (BrainNet Viewer, RRID:SCR_009446). After excluding recording

sites that were clinically determined to be a source of seizure (see details below) the 858

recording sites were distributed as follows (**Figure 2.3**): frontal (7 participants , 253 in

left hemisphere, 68 in right hemisphere), temporal lobe including medial temporal lobe

(10 participants, 218 in left hemisphere, 148 in right hemisphere), insula (4 participants, 8

in left hemisphere, 20 in right hemisphere), occipital lobe (3 participants, 13 in left

hemisphere, 33 in right hemisphere), parietal lobe (7 participants, 39 in left hemisphere,

28 in right hemisphere), and basal ganglia (4 participants, 23 in left hemisphere, 7 in

right hemisphere) (**Table 2.1**).

Subject ID	Electrodes location	Gender	Age	Nb. Recording sites
1	Bilateral temporal	Male	44	28
2	Left. Grid: frontal and temporal. Depth: frontal	Female	36	114
3	Bilateral frontal, temporal, insular	Female	33	115
4	Bilateral temporal, occipital. Right frontal	Male	19	68
5	Bilateral frontal, temporal, insular	Female	45	132
6	Right: temporal, occipital. Left: frontal, temporal, insular	Male	30	109
7	Bilateral occipital. Left temporal.	Male	32	45
8	Left temporal	Female	41	18
9	Bilateral frontal, temporal, insular	Male	14	96
10	Left: frontal, temporal, insular	Male	21	81
11	Bilateral temporal	Female	56	52

<u>Table 2.1. List of subjects and electrodes location</u>.
The table shows the distribution of 858 recording sites across subjects and brain regions. Unless otherwise specified to be grids, electrodes are depth electrodes. Note that the nomenclature of electrodes is broad; a frontal electrode goes from a deep brain region within frontal lobe up to frontal cortex. A temporal electrode goes from amygdala or hippocampus up to temporal cortex. Insular electrodes go from either anterior insula to frontal cortex or posterior insula to parietal cortex. And occipital electrode goes from medial occipital regions to occipital cortex and sometimes to parietal cortex.

2.2.3. Recording apparatus

LFP data were recorded using an XLTEK EEG system (Natus Medical, Inc.). Sampling frequency varied across participants between 1-2 KHz. Recordings collected with 2 KHz sampling rate were downsampled to 1 KHz for consistency of analysis across all 11 participants.

2.2.4. Experimental procedure

Participants sat upright and viewed a laptop screen during the course of the experiment. The screen was positioned at eye-level at a distance from the participants of about 40 cm. Participants were encouraged to pause and take a break at any point during the experiment if they felt fatigued or distracted.

2.2.5. Synching stimulus and LFP time series

In order to align the time of presentation of each experimental stimulus with the recorded brain signals a photodiode was attached to the bottom right corner of the screen. Each stimulus frame displayed a small white box at the location of the photodiode at stimulus onset, and a small black box at stimulus offset. Leads from the photodiode were inserted into the same bedside pre-amplifier used to record brain signals. The photodiode timeseries (a series of on-off pulses) was then used to synchronize the brain signals with stimulus onsets and offsets (Rorden and Hanayik, 2014) offline.

2.2.6. Experimental design

Patients fixated on a dot at the center of the laptop screen throughout each experiment. Each experiment consisted of a stream of natural scenes that prominently displayed either a human face, a building, or a car. Each image was displayed for 500 ms, followed by an interstimulus interval (ISI) of 1000 ms. During ISIs a blank screen (luminance set to average luminance of all images) was displayed; participants maintained fixation throughout each ISI.

Images were displayed in 9-15 blocks of 30-50 images each. All images were unique and none of the images were repeatedly displayed. A total of 450 images were displayed. At the start of each block participants were instructed to attend either the "face" images, the "car" images, or the "building" images. The attended category was fixed during each block; it alternated across blocks in the following order: building, face, car (**Figure 2.1**). After a random number of selected ISIs during each block a large question mark was displayed (an average five question marks was displayed per block). Participants were instructed to then verbally indicate if the last seen image was of the same category as the attended one. The experiment provided verbal feedback on their response to indicate correct and incorrect trials. All participants gave correct responses on at least 90% of the trials.

Given that all images belonged to one of three attended stimulus categories, the experiment was composed of nine distinct task conditions, each corresponding to a distinct (attended category, seen category) pair. These task conditions are illustrated in **Figure 2.1**.
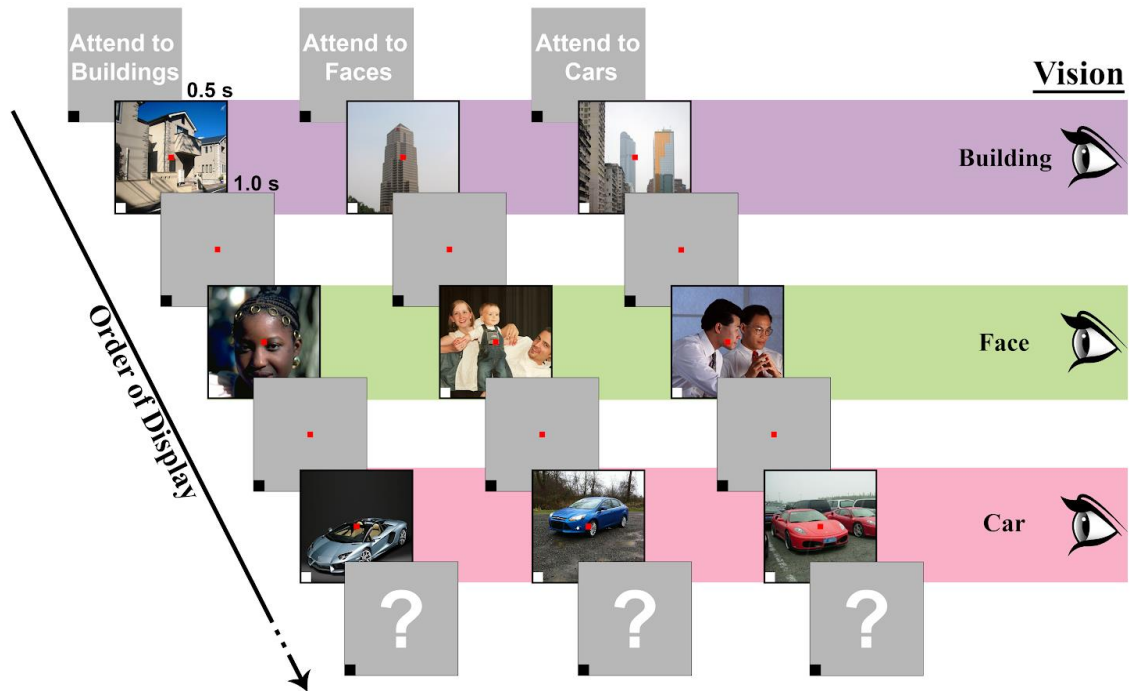
Figure 2.1. Experimental design to study category-based visual attention.
Participants viewed color photographs depicting either a car, building, or face.
Photographs were presented for 0.5 sec followed by a 1.0 sec grey screen inter-stimulus
interval (ISI). An experiment was partitioned into blocks of 30 to 50 photographs. At the
beginning of each block, participants were cued to attend to one object category in the
following order: building, faces, and cars. Photographs did not repeat across or within
blocks. At random intervals participants were presented with a question mark after the ISI
and asked to verbally indicate whether the last displayed photograph belonged to the
attended object category. This design allowed the study of 9 combinations of seen and
attended object category (for example "see building, attend car"). In the illustration
above, columns indicate series of photographs presented within one block. The attended
object category is indicated at the top of each column. Photographs were selected to
illustrate each of the 9 possible combinations of seen (rows) and attended (columns)
object categories.

2.2.7. Signal screening and preprocessing

Prior to analyzing brain signals we screened all recordings to identify recording sites suspected by each patient's clinical team to be near a locus of seizure-related activity, and recording sites corrupted by large artifacts that were obviously not related to healthy brain activity. We also excluded recording sites located above the surface of the brain, as identified by inspecting the post-op structural images. A total of 286 out of 1144 recording sites were excluded in this way.

After screening, all signals were referenced to a global mean. That is, for each participant independently a global average timeseries was computed and subtracted from the timeseries of each individual recording site.

2.2.8. Peri-stimulus power spectral density functions

For each recording site, the LFP starting from stimulus onset and ending 500ms after (i.e., the total duration of each stimulus display) was extracted and used to estimate a PSD function (Miller et al., 2014; Miller et al., 2016). PSD frequencies ranged from 1Hz (DC offset was excluded) to 100Hz with increment of 1Hz; frequencies between 56 and 63Hz were excluded to compensate for a 60Hz line artifact. Each of these single-trial PSDs were normalized by calculating the logarithmic value of dividing single-trial PSDs over the mean power of all single-trial PSDs ($\log[PSD/\langle PSD\rangle]$, where $\langle\cdot\rangle$ indicates an average across all trials for the given recording site) as in (Miller et al., 2016) Single-trial PSDs for each recording site were then grouped according to task condition (i.e., according to the [attended category, seen category] pair associated with each trial) and averaged to construct a condition-specific average PSD. For each recording site this

process resulted in nine condition-specific average PSD functions. A baseline PSD was also calculated by averaging across PSDs prepared from the first 500ms of signal during each ISI. Thus, a total of 8580 condition-specific PSDs were calculated from 858 recording sites across 11 participants.

2.2.9. Principal Component Analysis

The 8580 PSDs were treated as independent 93-dimensional (one dimension for each of the frequencies in the PSD) observation vectors in PCA. This resulted in 93 orthogonal spectral components. Each spectral component was itself a 93-dimensional PSD function, with each value indicating power at each of the studied 93 frequency points. In this work we study the top 3 components, which accounted for roughly 40% of the variance.

2.2.10. PC-specific encoding models

We investigated how variations in spectral power along each PC encoded information about variation in task conditions by constructing PC-specific encoding models. Encoding models were constructed independently for each recording site and participant. To construct models for participant k we first applied PCA to the PSDs from the other 10 participants. We then projected the *single-trial* PSDs for participant k onto the first, second, and third PCs resulting from this participant-specific PCA. Thus, for each recording site we have 450 projections (one per experimental stimulus) per PC describing variation in spectral power along the PC. These projections are the "responses" that are predicted by each PC-specific encoding model. Formally, for a

single recording site and participant let $\boldsymbol{q}_i$ be the PSD calculated for trial i and let $\boldsymbol{p}_j$ be the jth principal component. Then $r_{ij} = \boldsymbol{q}_i \cdot \boldsymbol{p}_j$ is the single-trial response for PC_j that is predicted by each encoding model. The encoding model for a single recording site in participant k is specified as a simple linear combination of task conditions:

$$r_j = S\boldsymbol{w}^T + b + \varepsilon$$

where $\boldsymbol{r}_j$ is an $(N_{train} \times 1)$ vector of "responses" along PC_j, S is the $(N_{train} \times 9)$ design matrix of the experiment (each column indicates a task condition), $\boldsymbol{w}$ is (9×1) vector of condition weights (i.e., regression parameters), b is an intercept term, and is ε zero-mean Gaussian noise. The number N_{train} indicates the number of training samples.

The values of the encoding model weights $\boldsymbol{w}$ and intercept b were determined for each recording site via simple linear regression. Regressions were performed by applying a *10-fold* leave-*k*-out procedure to a subset of *360* trials that were used only for training and evaluating encoding models (the remaining N_{val}= 90 trials were used for decoding analyses as described below). This means that for each recording site, *10* separate regressions were performed. Each regression used a different set of $N_{train} = 288$ trials that were randomly sampled from the *360* trials used to construct encoding models. On each of these *10* folds, the regression model was evaluated on the remaining $N_{test} = 72$ trials. We used Pearson correlation between model predictions and the observed responses $\boldsymbol{r}_j$. The "prediction accuracy" that we report for each encoding model is the average Pearson correlation across all *10* folds. Here an encoding model is considered "accurate" if the Pearson correlation exceeds a significance threshold ($p < .05$) determined by a random permutation test (permutation of prediction and observed responses across trials). The

encoding model weights that we discuss and analyze below are the average of the weights across all *10* folds.

2.2.11. Tuning width of encoding model

For analysis of tuning width encoding model weights for each recording site were normalized to span a (0.0, 1.0) range and then ranked by magnitude. Tuning width is the rank of the lowest-ranking weight that has a value of greater than 0.5. A "sharply" tuned encoding model would have a tuning width of 8, indicating only a single weight exceeds the middle of the (normalized) range of weight values. A "broadly" tuned encoding model would have a tuning width of 4 or 5, indicating an even distribution of weights about the middle of the range. Tuning width is shown in **Figure 2.6** by plotting weight value against weight rank. For the extreme case of broad and completely non-specific tuning the resulting plot would appear as flat line. For recording sites with highly-specific encoding of a subset of task conditions these plots will reveal curves with a sharp peak (corresponding to the largest model weight) and rapid fall-off.

2.2.12. Model-based decoding analysis

A decoding analysis was performed on the $N_{val} = 90$ trials that were not used to estimate or evaluate the encoding models. Decoding analyses were performed using data from participants S6-S11 only, as these were the participants for which the largest common number of trials (consisting of *432* trials) was acquired.

Here, the decoding objective is to predict the seen or attended stimulus category associated with a set of responses sampled from a population of recording sites. Decoding is performed independently for each PC. As above, a "response" r_j associated with the jth PC, $\boldsymbol{p}_j$ is defined as the projection of a PSD $\boldsymbol{q}$ onto the PC, $r_j = \boldsymbol{q} \cdot \boldsymbol{p}_j$. Below we will suppress the subscript j, as it is understood that all responses refer to a specific PC.

Let *s1, s2, s3* indicate the seen stimulus categories of "face", "building", and "car", respectively. To decode a seen stimulus category, say *s2*, we first form a response vector r_{s2} associated with category *s2*. Thus, for each recording site in the population, we randomly select a trial associated with the category *s2* under each attention condition. We then concatenate these trials across all recording sites. For example, to form a response vector associated with the seen category "*building*", we randomly sample for each recording site a trial associated with "see building, attend face", "see building, attend building" and "see building:attend car". Thus

$$\boldsymbol{r}_{s2} = (r_{s2:a1}^1, r_{s2:a2}^1, r_{s2:a3}^1, \dots, r_{s2:a1}^M, r_{s2:a2}^M, r_{s2:a3}^M)$$

where the superscript indexes a recording site, *M* is the total number of recording sites in the population, the subscripts *a1, a2, a3* index the three attended categories "face", "building", "car", and the notation *s2:a1* indicates a trial associated with "see building, attend face", and so on. The length of a response vector for a given seen stimulus category is thus $3M$. Note that response vectors for attended category can be formed in a similar way, by fixing the attended category and allowing the stimulus category to vary.

To perform model-based decoding of seen stimulus category from a response vector, say r_{s2}, we use the encoding model for each recording site in the response vector

to generate a *predicted response vector* r'_{s1}, r'_{s2}, r'_{s3} for each of the 3 possible stimulus

categories. We then calculate a Pearson correlation between the response vector r_{s2}, and

each of the predicted response vectors r'_{s1}, r'_{s2}, r'_{s3}. Decoding is successful if the

correlation between the response vector and its matching *predicted* response vector is

higher than the correlation the between response vectors and the other two, non-

matching, predicted response vectors. In this example, decoding would be successful if

the correlation between r_{s2} and r'_{s2} were larger than the correlation between r_{s2} and r'_{s1},

and also larger than the correlation between r_{s2} and r'_{s3}. We refer to successful decoding

of a response vector as a "hit".

To calculate the decoding performance for seen stimulus categories we formed

300 response vectors for each seen stimulus category, for a total of 900 response vectors.

Decoding performance is the number of "hits" divided by the total number of response

vectors. Chance performance is 33%, since each response vector has a ⅓ chance of being

successfully decoded by randomly selecting a seen stimulus category. Decoding

performance for seen stimulus category was calculated independently each PC.

To perform model-based decoding of attended stimulus category response vectors

r_{a1}, r_{a2}, r_{a3} were correlated with *predicted* response vectors r'_{a1}, r'_{a2}, r'_{a3} as described

above. Performance was calculated by counting "hits" across # response vectors, as

described above. Decoding performance for attended stimulus category was calculated

independently for each PC.

As shown in **Figure 2.9**, decoding performance was calculated for populations of

varying sizes (i.e., populations with varying numbers of recording sites) ranging from 1

to 401 recording sites. To select recording sites for a population of a given size all recording sites were rank-ordered according to their prediction accuracy. Thus, the population of size 1 contained the single recording site with the highest prediction accuracy. The population of size 2 contained the recording sites with the highest and second-highest prediction accuracy, and so on. We emphasize that *none* of the trials used to measure prediction accuracy were used to measure decoding performance.

2.2.13. Statistical analysis

Statistical analyses were performed using MATLAB 2018b (Mathworks, MA) and Graphpad Prism 8 (GraphPad Software, CA). Permutation tests were performed for enrichment analyses and comparisons to random distributions. PCA analysis was performed as described above. One-sample t-test was used to compare accuracy of decoding models to random, and student's t-test was used to compare accuracy of decoding between vision and attention. Unless otherwise specified, statistical significance is reported at $\alpha < 0.05$.

2.3. Results

Eleven participants performed a category-based visual attention task, where they were instructed to look at photographs of buildings, cars, and faces shown for 500 msec and followed by ISI for 1000 msec while attending to one of those three categories at a time. The design of the experiment allows the study of nine combinations of attended/seen categories.

2.3.1. Broadband and narrow, low-frequency components explain almost half the variance in spectral power across seen and attended stimulus categories

To determine the combinations of frequency bands that explain the most variance in spectral power across seen and attended categories we first prepared single-trial, peri-stimulus power spectral density functions (PSD) for each recording site in the dataset (858 number of recording sites across 11 participants). Single-trial PSDs were log-transformed and normalized ($\log [PSD/\langle PSD \rangle]$ where $\langle \cdot \rangle$ indicates an average across all trials for the given recording site; (Miller et al., 2016)). Normalized PSDs were then grouped according to the combination of seen and attended category associated with each trial, and then averaged within-group. This resulted in 9 normalized mean PSDs, one for each pair of seen stimulus category and attended stimulus category. An additional PSD corresponding to an average across all the inter-stimulus intervals was also prepared.

PCA analysis was performed on pooled data from all participants except the studied participant as described in the methods. We found that variance was rather broadly distributed across PCs (**Figure 2.2C**), with the top three PCs accounting for less than half (41.7%) of the total variance in spectral power (**Figure 2.3** bottom left). PC1 (24% of total variance) had a broadband profile indicated by elevated (non-zero) power across at all frequencies in the studied range (1-100 Hz). PC2 (8.8%) and PC3 (7.9%) had narrow, low-frequency profile as indicated by non-zero power over a narrow frequency range. Specifically, PC2 concentrated most non-zero power in a $\delta - \theta$ frequency range (1-8 Hz). PC3 concentrated non-zero power primarily in a $\alpha - \beta$ frequency range (8-30 Hz). PCA applied to single-participant data revealed some variation in the ranking of the

top three PCs (**Figure 2.3**), but the basic motif of one broadband and two narrow, low-frequency components were conserved across participants. Thus, as seen and attended categories varied in our experiment the largest variation in spectral power was along a broadband component (corresponding roughly to a variation in the sum power across all frequency components), while the second and third largest variations in spectral power were restricted to low (sub-gamma) frequencies.
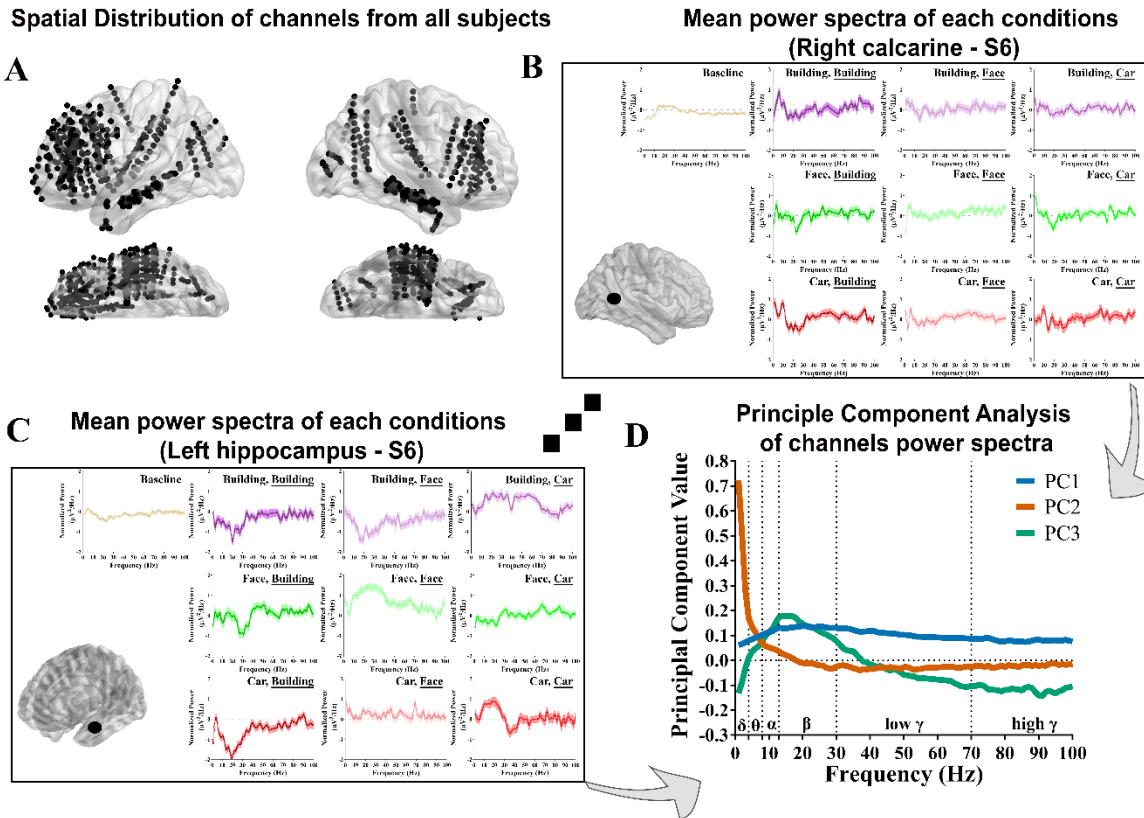
Figure 2.2. Principle component analysis (PCA) of peri-stimulus power spectral density (PSD) functions.

(**A**) Brain maps illustrating the location of all recording sites from 11 participants. Each black dot in the brain map in the top left indicates the location of one recording site, plotted in MNI space. (**B,C**) Peri-stimulus PSDs from a single recording site in the right calcarine cortex (B) and left hippocampus (**C**) from participant 6. Each sub-plot shows the average (shading indicates SEM) normalized, log-transformed PSD corresponding to each combination of seen and attended object category and for the ISI (attended object category is underlined in each subplot). These condition-specific averages were performed over all single-trial PSDs for a specified combination of seen and attended category (or for the ISI). Single-trial PSDs are derived from the local field potential (LFP) beginning at onset of stimulus for a duration of 0.5 sec. A total of 8580 condition-specific PSDs were calculated from 858 recording sites across 11 participants. (**D**) Results of PCA applied to all condition-specific PSDs. The top three principal components (PCs) are shown (labeled PC1, PC2, and PC3). PC1 characterizes broadband variation in spectral power; PC2 and PC3 are selective for power variation in narrow, low-frequency bands.
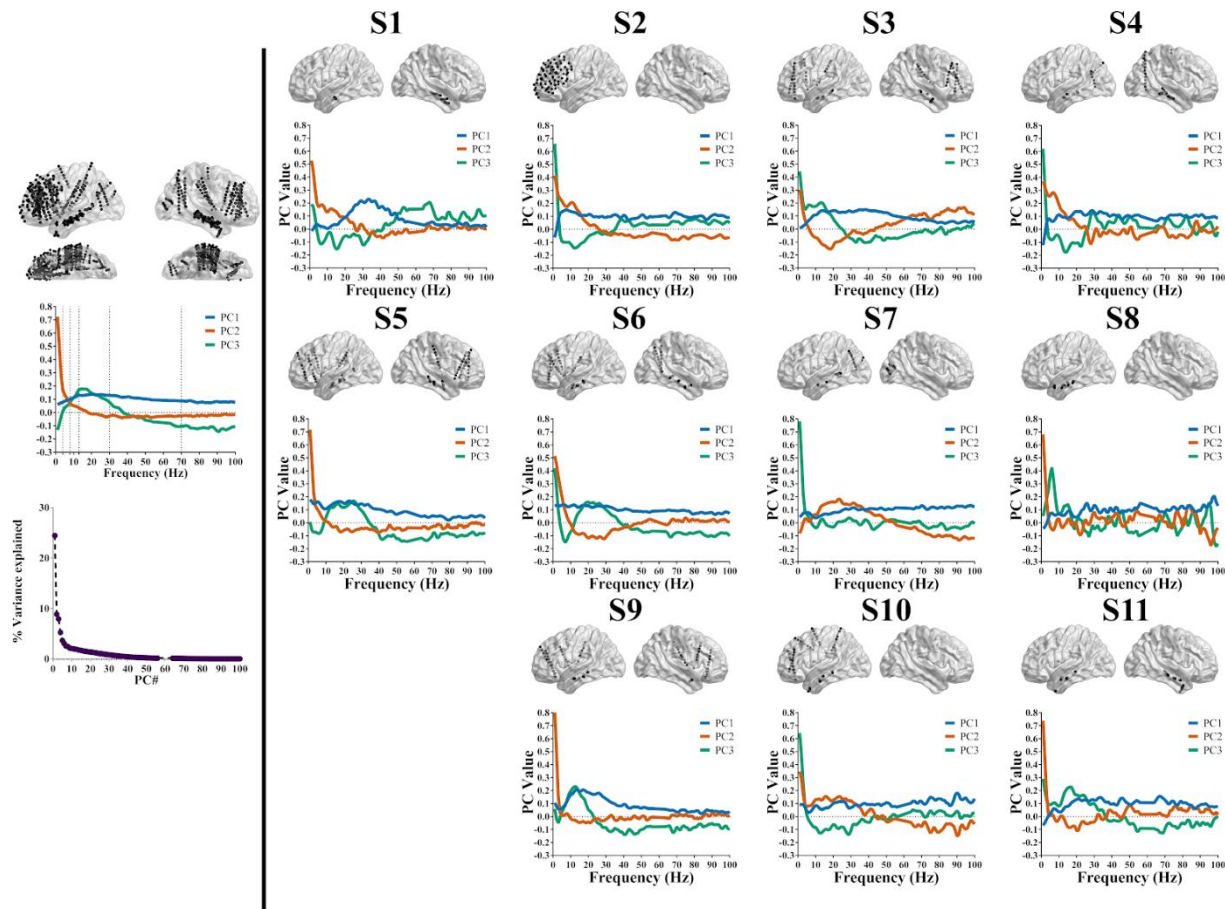
Figure 2.3. Subject based PCA analysis show similar results to the global PCA analysis applied on group of subjects

Upper left plot: The spectral patterns for the top three PCs are calculated based on condition-specific PSD from all participants except the tested participant to avoid double dipping. Lower left plot. PC1 is color coded in light blue, PC2 in orange, and PC3 in light green. Percentage of total variance explained by each PC shows that PC1 represents 24.4%, PC2 represents 8.8%, and PC3 represents 7.9%. All other plots: similar PCs' patterns are also broadly seen in the top three PCs calculated for each participant aside. Broadband PC1 is consistently broad across all participants, with a higher bump around 40 Hz for S1. As for PC2 and PC3, the pattern is broadly conserved with a low frequency (< 10 Hz) high power, and low frequency bump (roughly less than 30Hz). Note that the number of recording sites used for PCA analysis varies across participants between 28 and 132 recording sites. This variation account for the fluctuations we see in the plots of top three PCs. Also note the close percentage of representation of each of PC2 and PC3 in the lower left plot. This explains why the patterns in PC2 and PC3 calculated for each participant flips order for some participants like in S10. For each participant, above the individual plots of PC1-3, the corresponding distribution of recording sites across the brain (in black) of the participant is displayed with sagittal view.

2.3.2. Broadband and narrowband encoding explain a significant fraction of variance in the temporal lobe

In order to determine how information about seen and attended categories was encoded in each principal component, we independently estimated an encoding model for each of the top three PCs, and for each recording site. The encoding model predicts, for each trial, the spectral power along each PC as a function of the seen/attended stimulus category associated with the trial (**Figure 2.4A**). Thus, the encoding models used here were quite simple: for a given PC and recording site, a design matrix (independent variable) indicating the seen and attended category associated with each trial was regressed onto the projection the PSD onto the PC (see methods above). We estimated encoding models independently for each PC and recording site using linear regression. We evaluated the prediction accuracy of the encoding model for each recording site and PC by calculating the Pearson correlation between the model's predictions and the observed spectral power along the PC across a held-out set of testing trials (**Figure 2.4B**). For many recording sites this model achieves fairly high prediction accuracy (**Figure 2.4C-E**).

Example of channel-wise encoding using principal component projections
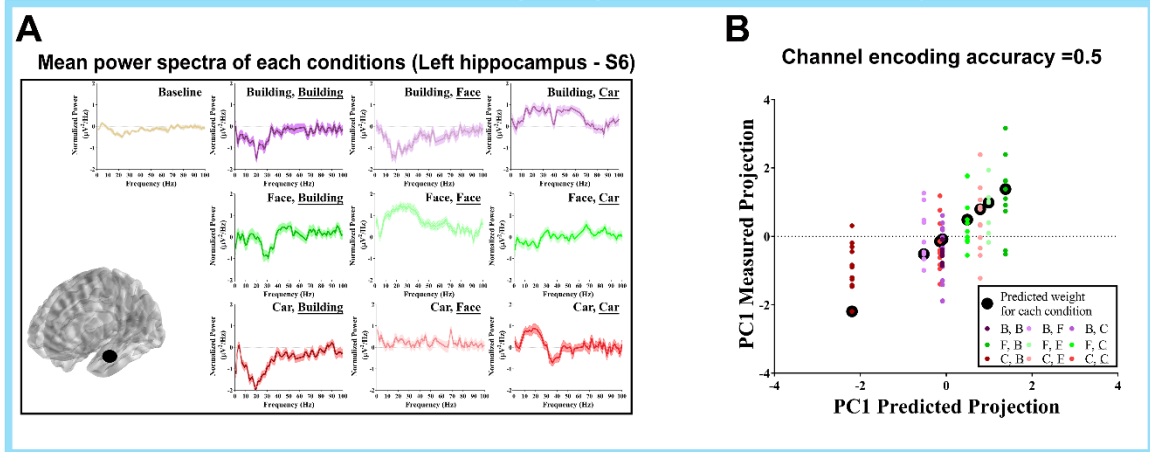
Spatial distribution of channels with accurate encoding model
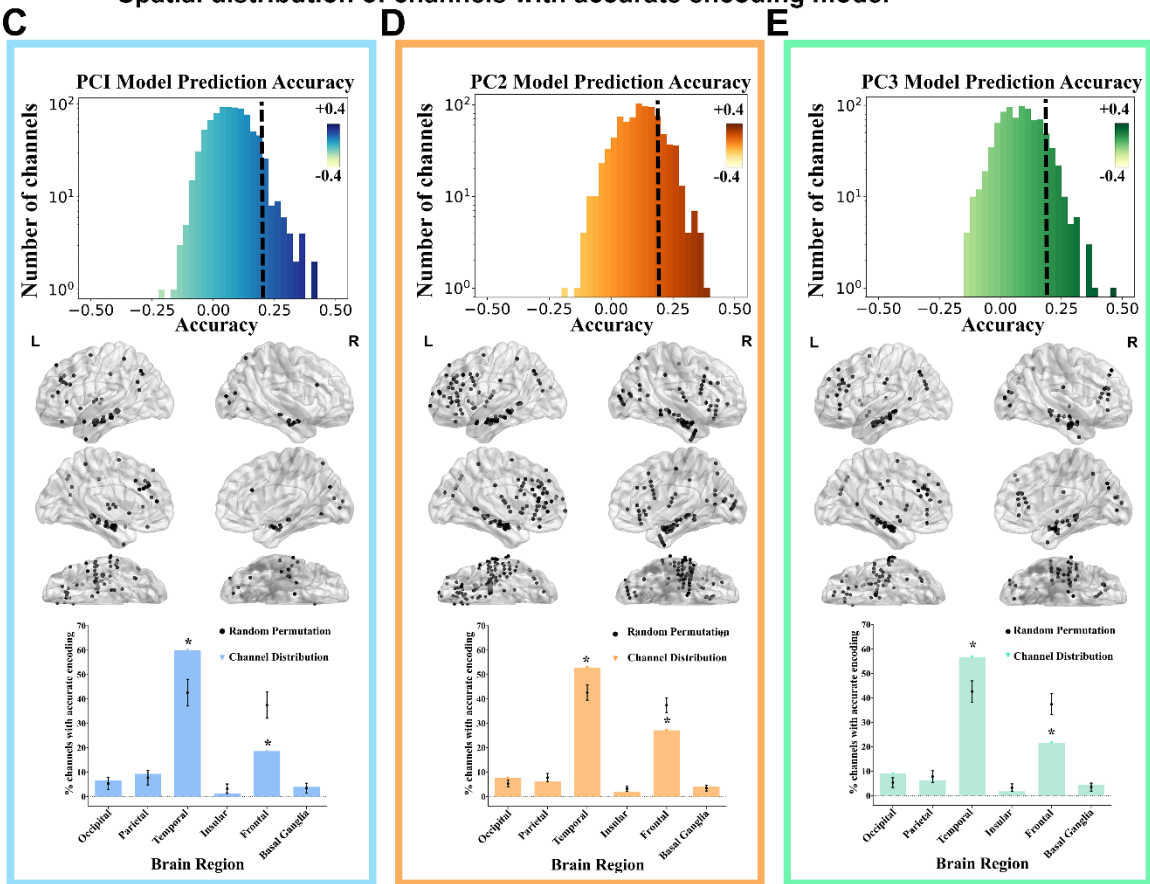
Figure 2.4. Spatial distribution of recording sites with an accurate encoding model for each PC

(A,B) Spatial distribution of recording sites with an accurate encoding model for each PC. (**A,B**) Condition-specific PSDs (**A**) at each recording site were projected onto each PC. Independently for each PC and recording site an encoding model was constructed. The encoding predicted power along each PC as a function of the 9 conditions in the experiment, where each condition is a pairing of seen and attended object category. This

panel shows the construction of an encoding model for the recording site illustrated in Figure 1. Our encoding model was evaluated for participant S6 as an illustrative example. (**A**) shows the predicted PSDs for a single recording site in the left hippocampus across the different attended/seen categories using the encoding model. (**B**) The PSDs predicted by the encoding model for each image in the test trials were projected over PC1, PC2, and PC3 and the projects were correlated with the actual projections of measured PSDs for the same trials. Shown in (**B**) is the correlation of predicted and measured projections for test trials over PC1 for a recording site shown in (**A**). The black dots represent the predicted projections for each category of test trials using the encoding model trained on an independent set of 80% of total trials whereas the colored dots represent the actual projections for each test trial. The different colors refer to different seen/attended category. The resulting recording site-wise predicted PC1 projection of each condition is used to calculate the encoding accuracy of the studied recording site; defined as the correlation coefficient between the predicted condition projections and the measured ones. (**C-E**) The same method described in (**B**) is applied to all 858 recording sites across all three studied PCs (PC1-PC3). Top panels: Histogram illustrating the distribution of recording sites by encoding accuracy for PC in log-scale (PC1 in blue, PC2 in orange, PC3 in green). The dashed line represents the accuracy threshold used to define accurately encoding recording sites. Middle panels: the spatial distribution of accurately encoding recording sites represents the anatomical distribution in the human brain presented in the MNI space across the 11 participants for PC1 (**C**, N=75 recording sites), PC2 (**D**, N=195 recording sites), and PC3 (**E**, N=111 recording sites). L: Left hemisphere, R: Right hemisphere. Significantly more encoding recording sites were observed for PC2 and PC3 compared to PC1 (**Figure 2.5**). Bottom panels: The corresponding distribution of the accurate encoding recording sites across the brain regions is plotted below the corresponding brain map where for each brain region the percentage of recording sites within the studied region encoding for the corresponding PC is indicated in corresponding colors of PC1 (light blue), PC2 (orange), and PC3 (light green). For each brain region, we assessed whether accurately encoding recording sites are specifically enriched (i.e. more than expected from initial distribution of all studied recording sites) using permutation analysis. Results of permutation are shown in black as mean +/- SEM. Only temporal lobe showed significantly more recording sites than random that accurately encode for PC1, PC2, or PC3. Permutation test with N=1000 iterations.*$p<10^{-3}$.

Encoding models were considered *accurate* if their prediction accuracy exceeded a common threshold (Pearson correlation > 0.19, *p* < .05; permutation test). Recording sites with accurate encoding models for all three PCs were identified in the temporal, prefrontal, occipital, insular and parietal cortex (**Figure 2.4C-E**). There were no recording sites within the precentral gyrus that showed accurate encoding for any of the 3 PCs (0/8 studied recording sites). We observed significantly fewer accurately encoding recording sites for PC1 compared to either PC2 or PC3 (**Figure 2.5A**), and a more distributed spatial pattern for PC2 and PC3 compared to PC1 (**Figure 2.5B**).

To identify brain areas in which accurate encoding of the seen and attended categories was enriched we compared the number of recording sites with accurate encoding models in each cortical lobe to the number expected if prediction accuracy for each recording site were randomly sampled from the empirical histograms in **Figures 2.4C-E**. We found that in the temporal lobe more recording sites than would be expected by such random sampling ($n = 45, 103, 63$ for PC1, PC2, PC3, respectively; $p=0.0009, 0.0006$ and 0.0001 permutation test) had accurate encoding models for PC1-3. In the prefrontal lobe, *fewer* recording sites than would be expected by such random sampling ($n = 14, 53, 24$ for PC1, PC2 and PC3, respectively; $p=0.0002, 0.0005$ and 0.0000, permutation test) had accurate encoding models for PC1-3. For all other lobes the number of recording sites that exceeded the prediction accuracy threshold was not statistically different from chance (**Figure 2.4C-E**, bottom panel).
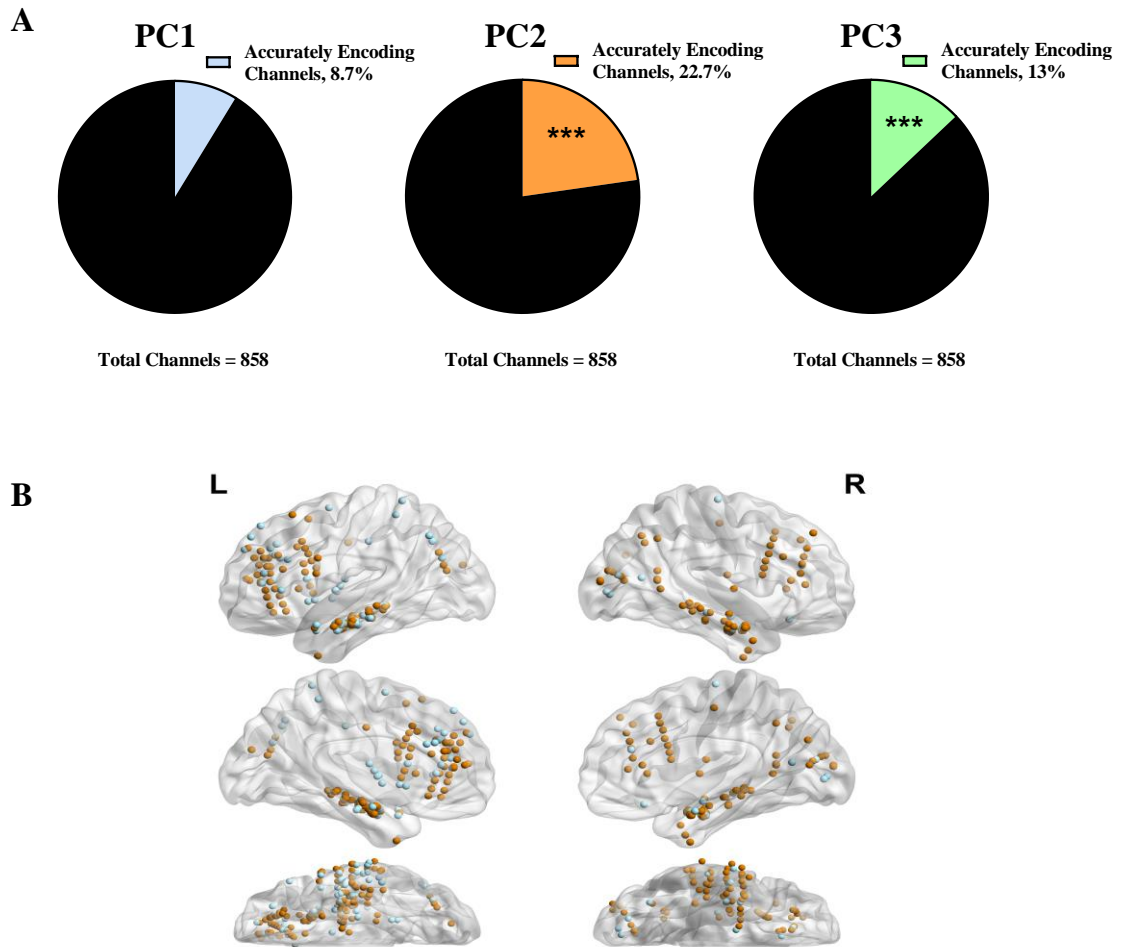
Figure 2.5. Spatial and spectral distribution of accurately encoding recording sites.
(A) Among total recording sites investigated at each PC, the pie charts show the proportion of accurately encoded recording sites for the studied PC. There was a significantly higher proportion of accurately encoding recording sites in PC2 and PC3 compared to PC1. Fisher exact test. N=848 total recording sites. ***p<0.001 comparing each PC to PC1. (**B**) Distribution of accurately encoding recording sites for PC1 (broadband pattern, light blue) and PC2/3 (narrowband pattern, orange) across the brain showing the more widespread distribution of accurately encoding recording sites in PC2/3 compared to the focal distribution in PC1.

To identify whether encoding of each of the three PCs is more prominent in specific brain region, we performed enrichment analysis to check whether accurately encoding recording sites are enriched in a specifically studied brain region using permutation tests. We found that in the temporal lobe more recording sites than would be expected by the distribution of studied recording sites (n = 45, n = 103, n = 63 for PC1, PC2 and PC3, respectively; p=0.0009, 0.0006 and 0.0001 permutation test) exceeded a threshold on prediction for all PCs. In the prefrontal lobe, *fewer* recording sites than would be expected by the distribution of studied recording sites (n = 14, n = 53, n = 24 for PC1, PC2 and PC3, respectively; p=0.0002, 0.0005 and 0.0000 permutation test) exceeded the prediction accuracy threshold for all PCs. For all other lobes the number of recording sites that exceeded the prediction accuracy threshold was not statistically different from chance (**Figure 2.4C-E**, bottom panel).

2.3.3. Broadband encoding model is more sharply tuned than narrowband encoding models

Are power variations along each PC equally dependent on all seen/attended categories, or only on select ones? To address this question we developed a selectivity index for each encoding model. Selectivity was defined as the rank of the encoding model parameter that exceeded the middle of the range of weight values. Note that each encoding model is specified by 9 parameters--one for each seen/attended category pair. A highly selective, or "sharply tuned" encoding model would have only one parameter at an extremum (a value well above or below the middle of the range). A non-selective or "broadly tuned" encoding model would have all parameter values uniformly distributed

about the middle of the range. By this measure we find that encoding models for PC1 are, as a population, significantly more sharply tuned than encoding models for PC2 and PC3 (**Figure 2.6A, Figure 2.7**). This was true when tested for all recording sites (**Figure 2.6B, Figure 2.7**) , and when tested for only recording sites in the temporal lobe (data not shown). Thus, of the top three principal components the one that is most sharply tuned, PC1, is the component that distributes power most uniformly across the spectrum. When PC1-selective recording sites in the temporal lobe were identified by the specific selectivity to which each recording site was tuned (face vs. building vs. car) (**Figure 2.8**), face-selective recording sites clustered within the fusiform gyrus and building-selective recording sites clustered within the parahippocampal gyrus (**Figure 2.8**).
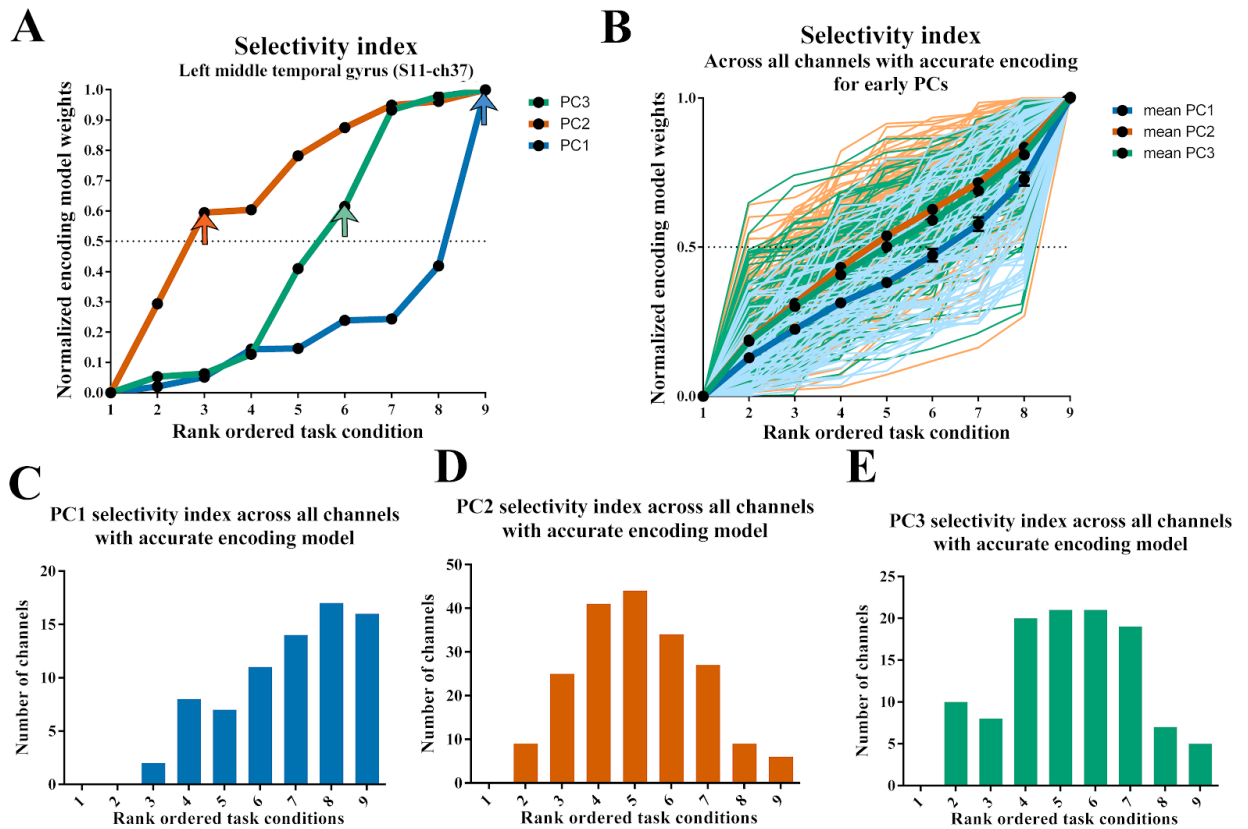
Figure 2.6. Sharpness of tuning to seen and attended object categories.
(**A**) Comparison of sharpness of tuning across three PCs for one recording site.
Parameters (normalized) of the encoding model for PC1-3 are plotted in blue, orange,
green, respectively. For each PC the parameters of the encoding model were rank-ordered
along the x-axis. The number rank of the smallest-valued parameter (arrows) above the
above the middle of the normalized range (dashed line at 0.5) was then identified. High
(8-9) or low (1-2) values of this response index indicate relatively sharp tuning. Mid-
range values (3-7) indicate relatively broad tuning. For the recording site shown here
from the left hippocampus (recording site 37) of participant S11, the index for PC1 is 9
(blue arrow), indicating sharp tuning of the response along the broadband component.
Indices for PC2 and PC3 are 3 (orange arrow) and 6 (green arrow), respectively,
indicated relatively broad tuning in the response along the low-frequency components.
(**B**) Rank-ordered tuning plots for every single recording site with an accurate encoding
model for PC1, PC2 and PC3 are plotted in thin line with color corresponding to the
studied PC. PC1: mean plotted in dark blue with SEM at each point. PC2: mean plotted in
dark orange. PC3: mean plotted in dark green. Responses along PC1 are on average
significantly more sharply tuned than responses along PC2-3. Statistical comparisons of
ranks is shown in **Figure 2.7**. (**C-E**) Histogram of the number of recording sites with
accurate encoding models for each of PC1 (**C**), PC2 (**D**), and PC3 (**E**) for each value of
the response index. Response indices for PC1 are skewed toward the extremum relative

to PC2-3, indicating sharper tuning of the broadband PC1 response than the low-frequency PC2 and PC3 responses.

Selectivity Index for each trial per PC
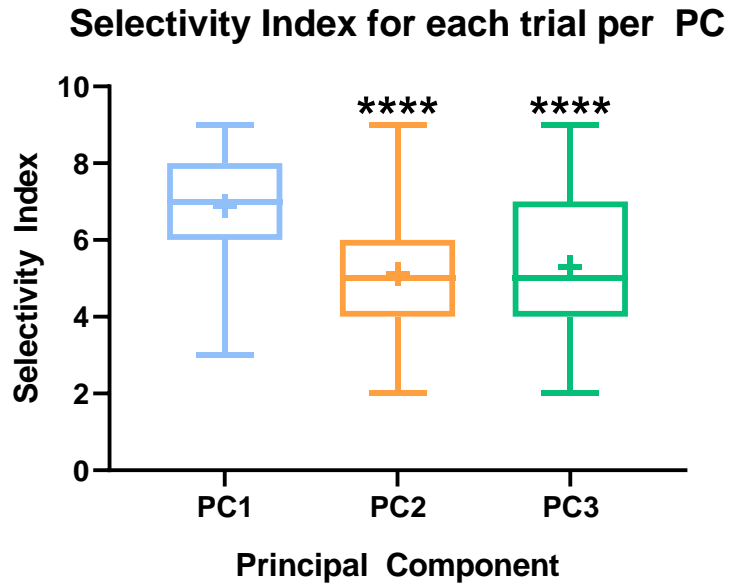
Figure 2.7. Comparison of selectivity index for each PC across all trials.

Box and whisker plot showing the median (line in box) and range of selectivity index for each PC across all trials. Mean is denoted by (+) sign. Rank order comparison was performed using Kruskal-Wallis test with Dunn's correction for multiple comparisons. N=75 (PC1), 195 (PC2) and 111 (PC3). ****P<0.0001 compared to PC1. Only significant comparisons are shown.

Selective and Accurate PC1 Channels

Selectivity Category:

Face

L   R

Selectivity Category:

Building

L   R

Selectivity Category:

Car

L   R
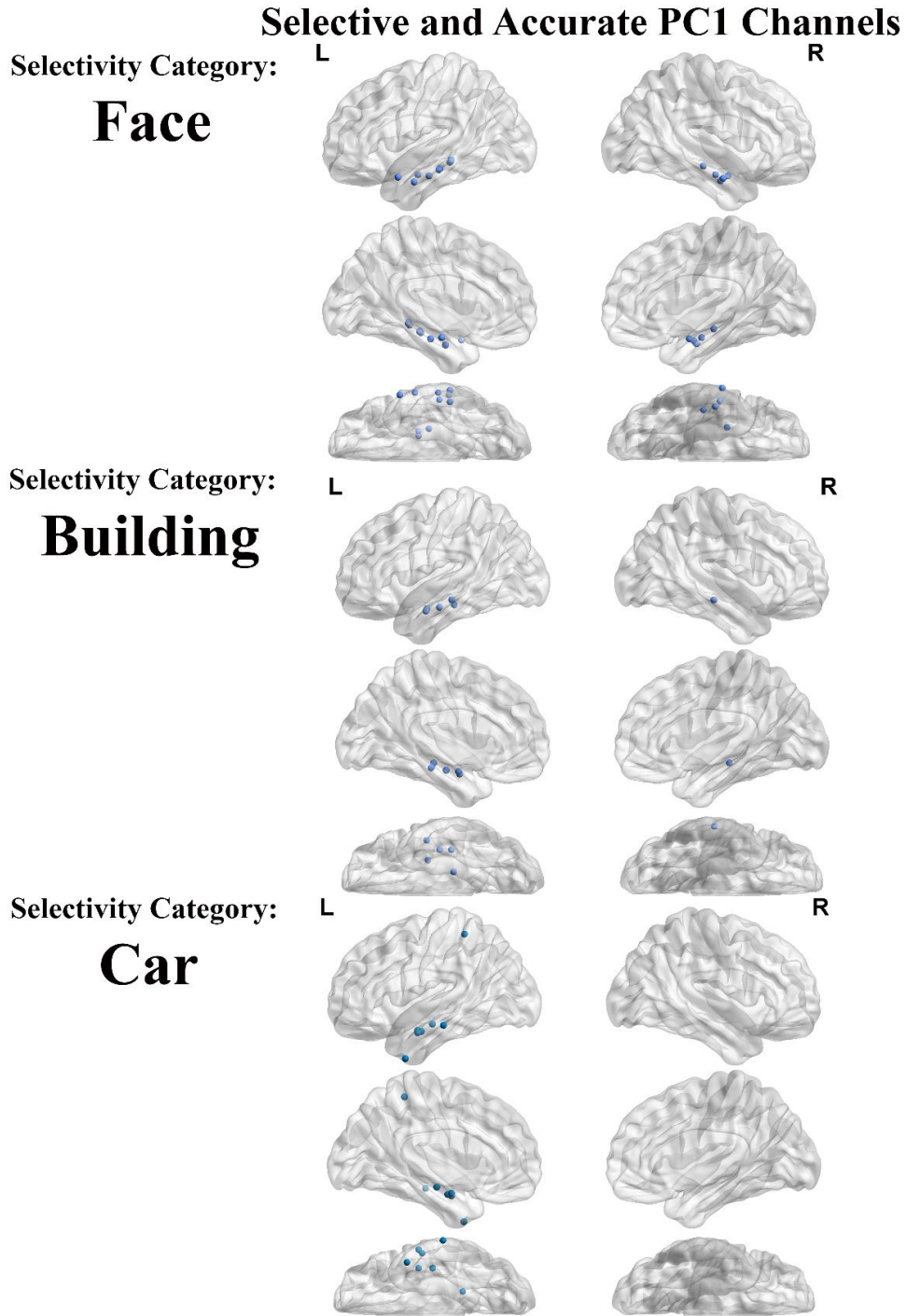
Figure 2.8. Spatial distribution of recording sites with accurate-encoding in PC1 and high selectivity index split by selectivity category.

Shown in light blue are dots representing each recording site that had accurate encoding on PC1 and was sharply tuned for a specific object category (Face, Building or Car) with selectivity index ≥ 7.

2.3.4. Information about seen and attended categories are unequally distributed across the top principal components

Given previous results (Klimesch, 1999; Klimesch et al., 2011; Miller et al., 2014; Jensen et al., 2015; Michalareas et al., 2016; Miller et al., 2016; Helfrich et al., 2017), we suspected that variations in spectral power along the top three PCs might encode different levels of information about seen and attended stimulus categories. Thus, we used a model-based decoding analysis to compare the amount of information about seen and attended stimulus categories encoded by each PC. This analysis used the encoding models to decode from measured brain activity the seen or attended stimulus category. The measure of brain activity in this case was the projection of each recording site's peri-stimulus PSD onto a single PC (i.e., the dependent variable of the encoding model for each recording site). Thus, the analysis allowed us to independently decode seen and attended stimulus category from variations in power along each PC. By comparing the accuracy of decoded seen stimulus category to the accuracy of decoded attended stimulus category we were able to quantify the relative amount of information each PC encodes about vision and attention (**Figure 2.9A-C**).

A PCI Model Prediction Accuracy

B

C Attention / Vision

D PC1 Decoding - All Channels

E PC1 Decoding - Temporal lobe

F PC1 Decoding - Occipital Lobe

PC2 Decoding - All Channels

PC2 Decoding - Temporal Lobe

PC2 Decoding - Occipital Lobe

PC3 Decoding - All Channels

PC3 Decoding - Temporal Lobe

PC3 Decoding - Occipital Lobe
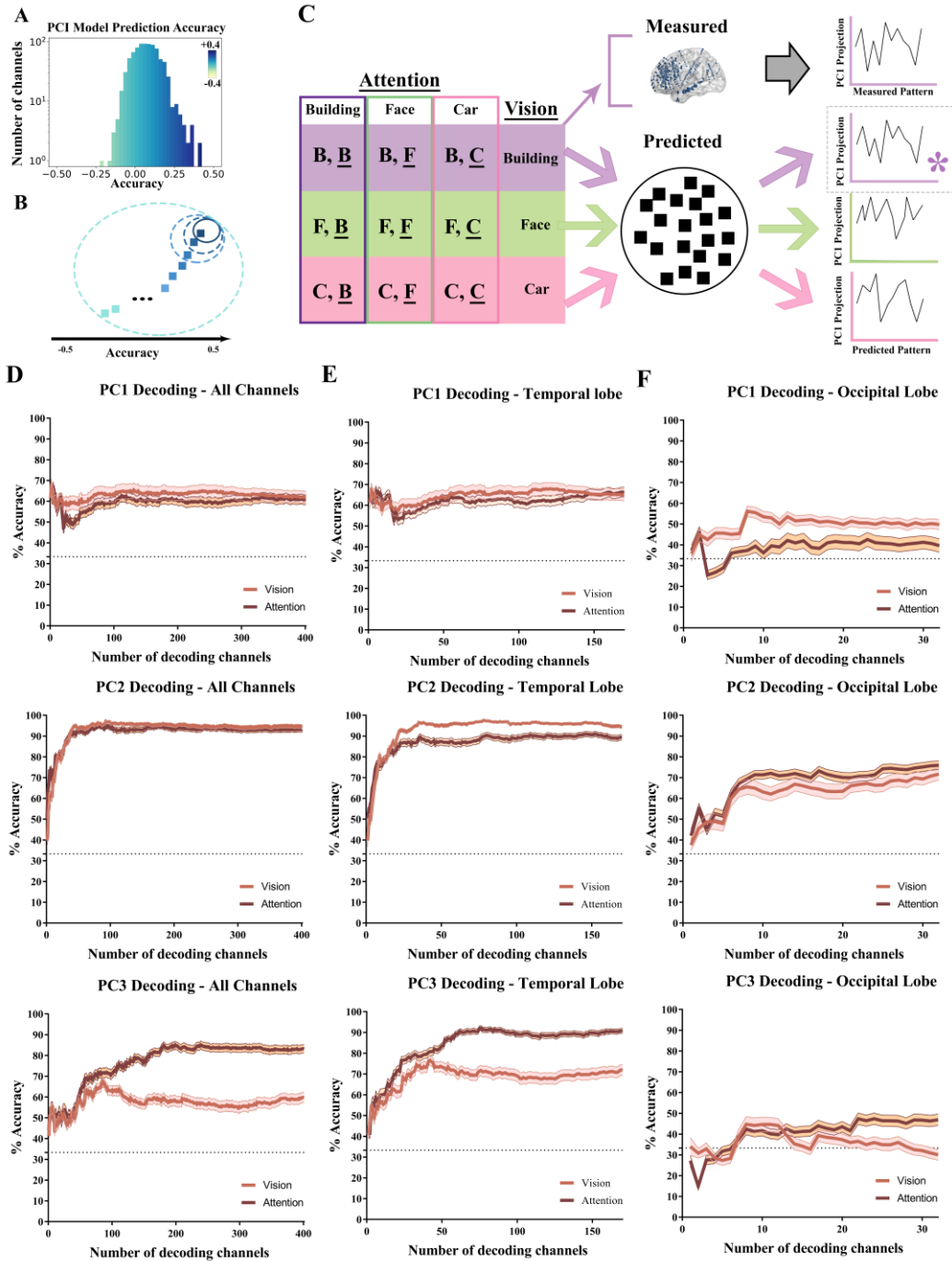
Figure 2.9. Model based decoding of seen and attended categories.
Model-based decoders were used to identify the seen or attended object category encoded
in spectral power along PC1, PC2, and PC3 from populations of recording sites. The
relative amount of information about seen and attended object category varies across PCs
and brain region. **(A-B)** How populations were selected. **(A)** Recording sites were selected
on the basis of their encoding model prediction accuracy. The plot shows a histogram of
encoding model accuracies for PC1 (similar histograms were constructed PC2 and PC3).
Color indicates prediction accuracy. **(B)** Populations of varying size were constructed by
selecting recording sites in order of encoding model prediction accuracy. The population

of size 1 (squares indicate recording sites; circles delimit populations) contains the single recording site whose encoding model has the highest prediction accuracy. The population of size 2 contains the recording sites whose encoding models have the highest and second-highest prediction accuracies, and so on. The largest population contains all recording sites. **(C)** The procedure for decoding seen object category from a population of recording sites (a similar procedure was applied to decode attended object category). The first three columns on the left of the matrix indicate the 9 different conditions of the experiment. Capital letters indicate the seen, attended object categories, where B=building, F=face, and C=car. Attended object category is fixed along each column; seen object category is fixed along each row. The rightmost column indicates the seen object category to be identified from measured spectral power (along PC1 in this example) in the population of recording sites. In this example, the "true" seen object category is building. Thus, measured spectral power was obtained from three randomly selected trials (top row of the matrix) in which the seen object was building and the attended object was car, face and building, respectively. Measured spectral power for each recording site and trial were concatenated to form the "measured pattern" illustrated by the plot at top right. In this plot recording site and condition are arranged along the x-axis, and measured spectral power is indicated on the y-axis. To decode seen object category from this pattern of measured spectral power the encoding model for each recording site in the population was used to generate "predicted patterns" (bottom three plots at right) corresponding to each of the three seen object categories. That is, for each seen object category predicted spectral power for each recording site is concatenated across the three attended object categories. Each of the three predicted patterns was then correlated with the measured pattern. If the predicted pattern corresponding to the true seen object (in this example "building", indicated with an asterix) was most highly correlated with the measured pattern, decoding was considered successful and marked as a "hit". **(D)** Decoding performance was estimated for spectral power measured along PC1 (top row), PC2 (middle row) and PC3 (bottom row). Columns indicate that recording sites were sampled from all available sites (left column), temporal lobe only (middle column **E**), or occipital lobe only (right column **F**). Each plot shows percentage of hits (y-axis) across 900 attempts (300 attempts per each object category) for populations of varying size (x-axis). Decoding of seen object category (red curves) and attended object category (brown lines) was performed independently. Statistical analysis is presented in **Figure 2.10**.

We observed a consistent pattern of differential decoding of information about seen and attended stimulus category regardless of whether brain activity was sampled from all lobes (401 recording sites) or the temporal lobe only (170 recording sites) when compared to random (**Figure 2.9D,E**). For PC1 and PC2 decoding accuracy for seen and attended stimulus categories was close to parity (**Figure 2.9D,E**, top and middle); however, given a sufficiently large (> 50 recording sites) population, PC3 decoding accuracy was significantly better for attended than for seen stimulus category (**Figure 2.9D,E**, Bottom). We observed a slightly different pattern when activity was sampled from occipital lobe only (32 recording sites): for PC1 only seen stimulus category could be decoded more accurately than chance (**Figure 2.9F**). Thus, the spectral power along the first (broadband) PC encodes *at least* as much information about seen as attended stimulus category; spectral power along the second $(\delta - \theta)$ PC appears to encode roughly the same amount of information about vision and attention; spectral power along the third $(\alpha - \beta)$ PC appears to encode significantly more information about attended than seen stimulus category (**Figure 2.9D-F**).
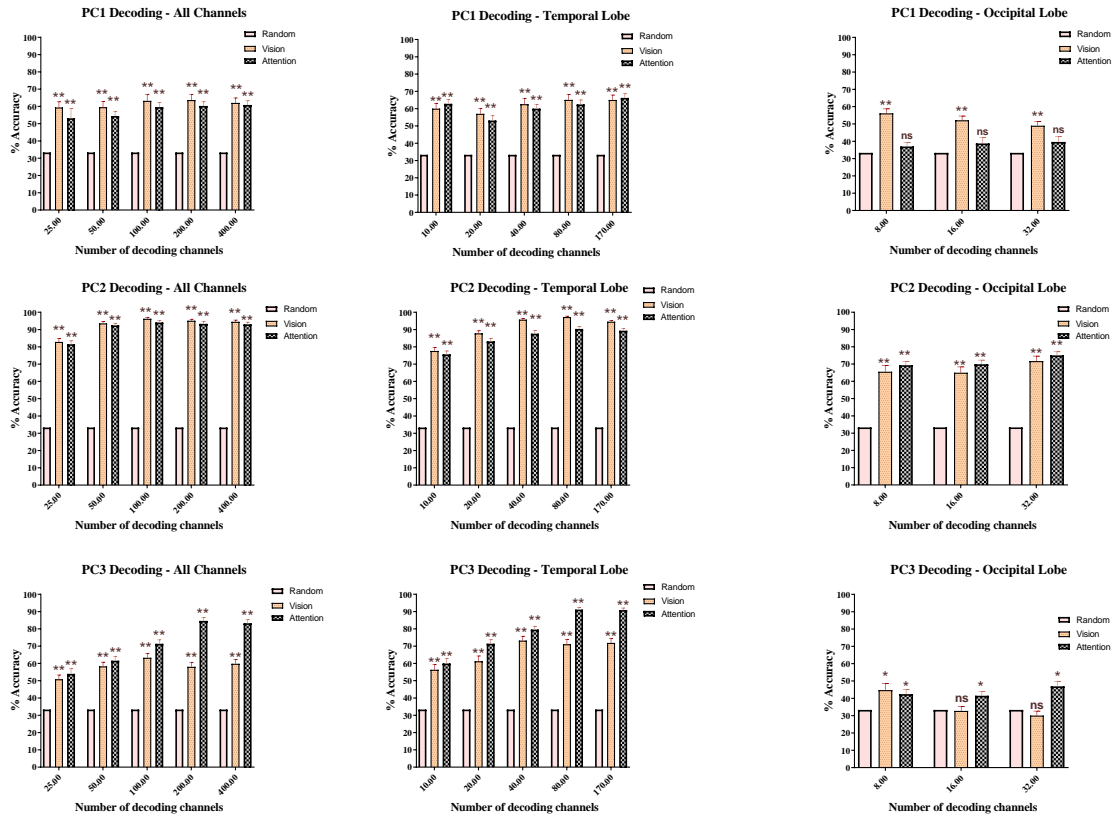
Figure 2.10. Comparison of decoding accuracy for each PC to random.

One-sample t-test used to compare each sample to random (33.33% accuracy) for decoding specific categories (face, building or car). *P<0.01, **P<0.0001.

2.4. Discussion

2.4.1. Summary of results

We analyzed how variations in the spectral power of local field potentials encode variations in seen and attended object category. Using PCA, we found that 40% of the variance in spectral power is explained by variation in broadband (PC1) power and by variation in low ($\delta - \theta$ for PC2, $\alpha - \beta$ for PC3) frequencies specifically. Power variation along the broadband and low-frequency PCs encoded information about variations in seen and attended object category at recording sites in occipital, temporal, insular, parietal and prefrontal cortex. Encoding was enriched in the temporal lobe, which is well-known to maintain representations of object identity and category.

Although broadband PC1 explained the single largest fraction of variance, it was less tightly coupled to variations in seen and attended stimulus category, as evidenced by the fact that fewer recording sites have an accurate PC1 encoding model than they do for the low-frequency PC2 or PC3 encoding models. This means that, relative to PC2 and PC3, a larger fraction of the variance explained by PC1 is not related to variations in seen or attended stimulus category. This "noise" may reflect variation in signal properties across different participants, different brain areas, or just the inevitable trial-to-trial variability of signals recorded at one site (which will be reflected in the SEM of the within-group average PSDs that are entered into the PCA).

For recording sites with an accurate PC1 encoding model, variation in power along the broadband PC1 was more sharply tuned than for the low-frequency PC2 and PC3. The selective tuning of power along the broadband PC1 is reminiscent of the selective BOLD responses to object category observed in temporal lobe (Bar et al., 2001;

Haxby et al., 2001). Indeed, previous work suggests that broadband LFP and the BOLD response are tightly coupled (Hermes et al., 2017).

Although information about seen and attended object categories was encoded by power variations along each PC, the relative amount of information about vision and attention varied across PCs. Broadband PC1 encoded slightly more information about seen that attended category. The $\delta - \theta$ band PC2 robustly encoded information about both seen and attended category. The $\alpha - \beta$ band PC3 encoded much more information about attended than seen categories.

2.4.2. Information about seen and attended object category is encoded by variation in power at many frequencies

Our findings are consistent with previous work that reported encoding of object category in broadband and low-frequency power variations. (Bosman et al., 2012; Miller et al., 2014; Jensen et al., 2015; Michalareas et al., 2016; Miller et al., 2016). In this work we studied the encoding of both seen and attended objects category across a spatially broad distribution of recording sites. We found that the encoding of attended object categories is, like the encoding of seen object categories, encoded by power variation in multiple spectral components.

We did not observe a spectral component that resembled a narrowband gamma response (Fries et al., 2008; Fries, 2009). The absence of an obvious narrowband gamma component doesn't mean that the gamma band is not an essential component of the neuronal processing of seen and attended object categories. Our findings simply indicate

that a narrowband gamma response did not account for enough of the variance in spectral power during our experiment to merit its own PC. Also notable is an absence of a spectral component resembling a broad (high-pass) gamma response (Jacobs and Kahana, 2009; Vidal et al., 2010). One possible explanation for this finding (Miller et al., 2014) is that broad, high-pass gamma responses reflect a broadband effect that is masked by a suppressed low frequency (sub-gamma) narrowband response. Therefore, by decoupling the broadband and low-frequency narrowband patterns, the PCA performed here unmasks the low-frequency components observed in PC2-3 and reveals the underlying broadband effect in.

Our results may be interpreted as endorsing an expansive, inclusive approach to analyzing the relationship between variations in spectral power and task conditions, particularly for tasks that involve interacting top-down and bottom-up signals. Focusing exclusively on a single frequency band, such as narrow-band gamma, may obscure components of the spectrum that encode a significant amount of information.

The approach we used to answer which frequency bands are subject to the most power variation upon varying the category of attended and/or seen object doesn't limit the study of PSD variance to certain frequency bands.

2.4.3. The broadband response

Our results provide a detailed characterization of the broadband response to seen and attend object categories. We now briefly summarize its most salient characteristics.

Broadband responses are promiscuous. Projecting a PSD onto the broadband components effects an equally-weighted sum of powers at all frequencies. Therefore, power variations at any frequency will register as non-zero variance along the broadband PC. This makes broadband power variations sensitive to both signal and noise, broadly construed. This is most likely why the broadband PC explains the most variance in PSDs but at the same time offers the fewest recording sites with an accurate encoding model.

Interestingly, where the broadband response is coupled to variation in seen and attended category (i.e., at recording sites with an accurate encoding model), it is more selective than low-frequency components (PC2-3). Of the three PCs, PC1 was the most sharply tuned. In the temporal lobe the recording sites where broadband response was selective for faces tend to locate more lateral than recording sites where the broadband response was most selective for buildings or cars, which in turn are medially located. This is generally consistent with relative locations of place and face selective regions revealed in fMRI studies (Kanwisher et al., 1997; Haxby et al., 2001; Joseph, 2001).

Across the population of recording sites studied here, broadband responses were quite redundant. This was evidenced by plots showing the change in decoding performance as a function of population size. Relative to the low-frequency PCs, decoding performance plateaued rapidly when decoding was performed with broadband responses. This observation held regardless of whether recording sites were sampled from only occipital lobe, only temporal lobe, or all available sites.

Finally, in early visual areas broadband responses during our experiment were "bottom-up". This was evidenced by the fact that recording sites in the occipital lobe permitted above-chance decoding performance for seen object category, but not attended

object category. In contrast, low-frequency PC2 responses in occipital lobe recording

sites permitted above-chance decoding of both seen and attended object category, while

PC3 responses in occipital lobe recording sites permitted above-chance decoding of

attended object only.

In summary, we find that broadband PC1 responses were promiscuous (i.e.,

sensitive to multiple sources of variance), sharply tuned, generally consistent with

findings from fMRI studies, encoded redundant information across the recording sites

studied here, and in occipital lobe encoded purely "bottom-up" sensory information.

2.4.4. Spectral signature of attention and vision

Although many previous studies have reported that attention modulates the

encoding of seen stimuli in firing rate (Moran and Desimone, 1985) and BOLD responses

(Cukur et al., 2013) we found no evidence that attention systematically modulated the

encoding of seen object category in power variations along any of the top three PCs.

Rather, we found that information about attention and seen stimulus category were

differentially distributed across PCs, as summarized above. This finding suggests that

attention and vision have different spectral signatures. In particular, variation in power

within the $\alpha - \beta$ band of frequencies (PC3) was highly selective for attended object

category. This finding is generally consistent with emerging evidence for asymmetric

encoding of top-down and bottom-up signals in variation of spectral power (Bastos et al.,

2015; Jensen et al., 2015; Kafaligonul et al., 2015; Michalareas et al., 2016).

CHAPTER THREE

DECODING OF THE VISUAL MENTAL STATE

3.1. Introduction

Visual mental imagery is a cognitive function that was shown to be spatially tightly correlated with vision in the human brain using fMRI (Kanwisher et al., 1997; Bartolomeo, 2008) and single neurons recordings (Kreiman et al., 2000a). This regional overlap between mental imagery and vision was also reported to be conserved across sub-modalities of vision including the "where" and "what" of objects that are impaired in both mental imagery and vision when the dorsal and ventral streams were respectively damaged (Levine et al., 1985). However, responses to mental imagery and vision do not fully overlap in human brain. Clinical series have been reported where patients had damage to vision, but had intact mental imagery or the opposite (Farah, 1984). Kreiman et al. (Kreiman et al., 2000a) showed studied whether mental imagery and vision share neuronal substrates at the level of single neurons within the medial temporal lobe and reported that although most of the studied neurons were responsive to both vision and imagination, there were some neurons that responded only to vision and other that responded only to mental imagery. The two main components of mental imagery, i.e. maintenance of mental imagery in working memory and recall, were studied at the spectral level (Jensen et al., 2007) showing a close association with an increase in gamma activity (30-100Hz) when studied using MEG, EEG, and LFP recordings (Sederberg et al., 2003; Gruber et al., 2004; Osipova et al., 2006; Sederberg et al., 2007). Theta (Sauseng et al., 2010) and alpha oscillations (Jokisch and Jensen, 2007) were also reported to be increased with the increase of memory load. Specifically, Van Gerven and his colleagues studied ECoG recordings (van Gerven et al., 2013) and showed that theta/alpha band (8-14 Hz) and gamma band (65–128 Hz)

modulations are associated with the stimuli-specific neuronal activity in different recording sites within the temporal lobe. However, studies from neuroimaging have demonstrated that cognitive control of mental imagery goes beyond the temporal and occipital lobes and involves large-scale network activity that includes the frontal, parietal and temporal lobe (Ishai et al., 2000; Ganis et al., 2004).

In this work, we studied the response of the brain to different visual mental states in order to better understand the encoding of visual mental imagery at a systems neuroscience level. We tailored our experimental design to allow for the comparison of the brain response to passive viewing of images, active looking at images to memorize them, and mental imagery of the memorized images. During passive viewing and ISI a simple attentional task was applied to discriminate between simple attentional state and mental imagery. We used principal component analysis to study the spectral patterns accounting for the most variation across visual mental states and across studied recording sites and subjects. We built both encoding and decoding models of the studied visual mental states using the candidate spectral patterns revealed by the PCA.

3.2. Material and Methods

3.2.1. Subjects

Thirteen epileptic patients (7 males, 6 females) with ages range between 18 and 58 participated in the experiment (**Table 3.1**). The subjects underwent surgical procedure for implantation of depth electrodes for detection of seizures within cortical and subcortical structures. The location of electrodes was solely determined based on clinical indication in

patients with refractory epilepsy. All subjects provided written consent approved by the

Institutional Review Board at the Medical University of South Carolina.

Subject ID	Electrodes location based on clinical target	Gender	Age	Nb. Recording sites
1	Right: frontal, temporal, insular	Male	37	66
2	Left: frontal, temporal, insular	Male	21	63
3	Bilateral: frontal, temporal	Male	58	79
4	Bilateral: frontal, temporal, insular	Male	30	93
5	Bilateral: frontal, temporal, insular	Female	53	122
6	Left: frontal, temporal, insular	Female	34	62
7	Bilateral: frontal, temporal, insular	Female	18	117
8	Left: frontal, temporal. Right: temporal, insular	Female	23	63
9	Bilateral: frontal, temporal, insular	Male	38	133
10	Bilateral: frontal, temporal, insular.	Male	40	103

	Left: occipital			
11	Bilateral: temporal, occipital	Female	31	72
12	Bilateral: temporal, occipital	Male	23	53
13	Right: frontal, temporal, insular	Female	34	65

Table 3.1. List of subjects and electrodes location.

The table shows the distribution of 1091 recording sites across subjects and brain regions. The electrodes are depth electrodes. Note that the nomenclature of electrodes is broad; a frontal electrode extends from a deep brain region within frontal lobe up to frontal cortex. A temporal electrode extends from amygdala or hippocampus up to temporal cortex. Insular electrodes extend from either anterior insula to frontal cortex or posterior insula to parietal cortex. Occipital electrodes generally extend from medial occipital regions to occipital cortex and sometimes to parietal cortex.

3.2.2. Electrode features, placement, and location mapping

The location of Ad-Tech subdural and depth electrodes varied among subjects and it is listed in **Table 3.1**. The placement of electrodes was solely guided by clinical evaluation of each subject and is mapped to the brain as shown in **Figure 3.1**. Each depth electrode has 10 recording sites separated along the electrode by 5mm. Each electrode has a diameter of 2.29 mm.
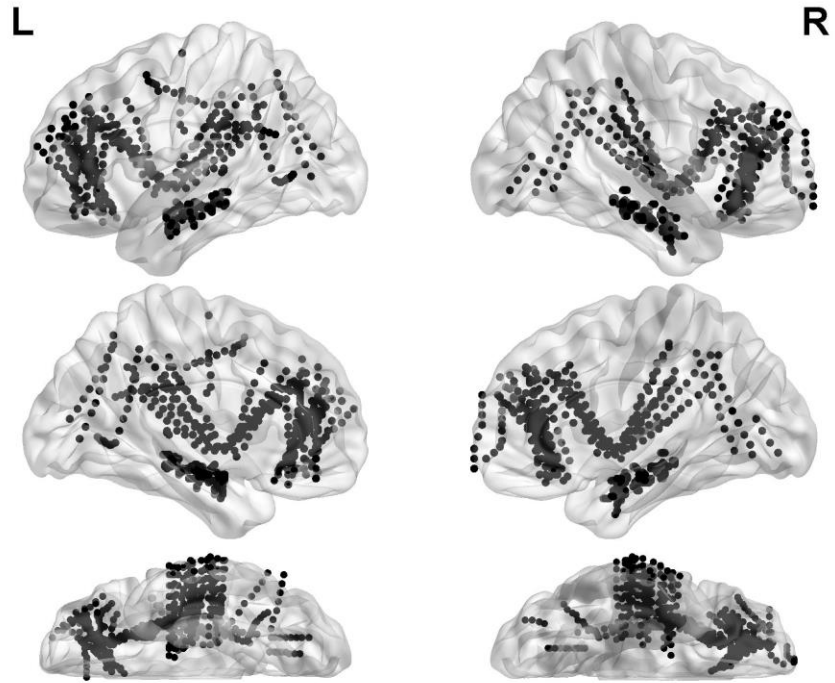
Figure 3.1. Brain maps illustrating the location of all recording sites from the 13 subjects enrolled in the study.

Each black dot in the brain map indicates the location of one recording site, plotted in MNI space.

3.2.3. Recording apparatus

LFP data were recorded using an XLTEK EEG system (Natus Medical, Inc.). Sampling frequency was 2 KHz across subjects. Recordings were downsampled to 1 KHz and all further analysis were applied on the downsampled recordings.

3.2.4. Experimental procedure

Subjects sat upright and viewed a laptop screen during the experiment. The screen was positioned at eye-level at a distance from the subjects of about 40 cm. Patients were encouraged to pause and take a break at any point during the experiment if they felt fatigued or distracted.

3.2.5. Experimental design

Patients were instructed to focus their vision, or fixate, on a dot at the center of the laptop screen throughout each experiment. Each experiment consisted of two phases:

1- In the first phase, subjects are instructed to fixate on a red dot in the center of the screen and to monitor if the dot changes its color. Then a stream of paintings that prominently feature either a human face, a landscape scene, or an abstract shape was displayed. Each image was displayed for 2.5 s, and followed by an interstimulus interval (ISI) of 2.5 sec. During ISIs a blank screen (luminance set to average luminance of all images) was displayed. Subjects maintained fixation throughout each ISI. All images were unique and none of the images were repeatedly displayed. A total of 45 images were displayed (**Figure 3.2**). After a random number of displayed images subjects were instructed to then

verbally indicate if the fixation dot changed color and, they were provided with feedback on their response to indicate whether they got it right or not. All subjects were correctly identifying the presence or absence of the color change. The subjects were asked about the color changes at nine instances, and the dot changes its color three times.

2- In the second phase of the experiment, the fixation dot doesn't change color, and subjects were instructed to memorize each image, one at a time, the to imagine the same image as long as the ISI is on. So this time the ISI is actually referred to in the text as mental imagery (MI). The same images were displayed (45 images), in the same order, and the same time (2.5 sec). MI time was displayed for 2.5 sec too (**Figure 3.2**). Instead of asking about a change of color at the fixation point, and at the same point in time as in the first phase, the subjects were asked to give a feedback about how vivid they were able to imagine the images during MI. In general, subjects reported that they were able to successfully imagine the displayed images during MI, with some minimal difficulties when the imagined images were abstract paintings.

This experimental design allows the comparison of recording sites responses to four different visual mental states: vision prior to ISI, ISI, vision prior to MI, and MI. These four states reflect passive viewing state, rest state, image memorization state, and MI state respectively.
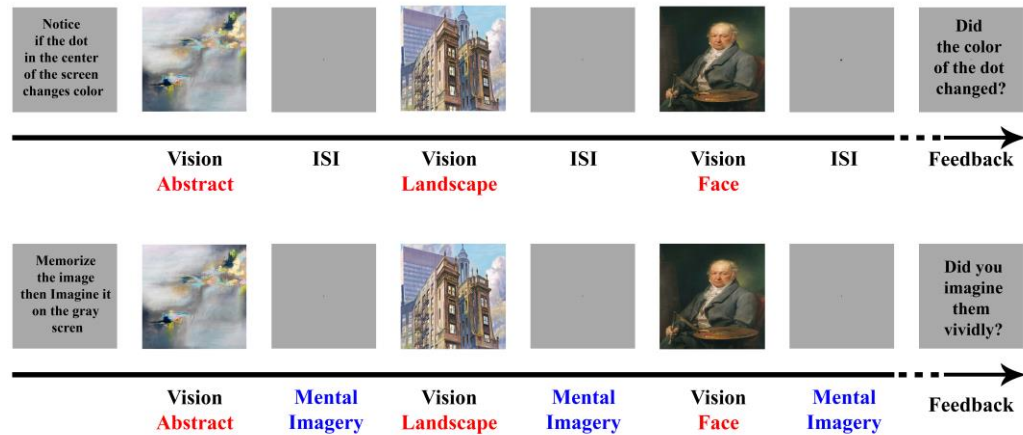
Figure 3.2. Experimental design showing the two phases of the study.
The figure shows the experimental design used to study visual mental state. In the first step (first row), subjects were instructed to look at images of abstract, building, and face paintings each displayed for 2.5 sec and followed by ISI (gray screen) for 2.5 sec and to notice if the dot in the center of the screen changes color from red to black. At a random time after the ISI the subject is instructed to give a feedback whether the color of the dot changed or not. Then in the second step (second row), subjects were instructed to memorize the displayed image on the screen, then to imagine it as long as the gray screen is on. The images are displayed for 2.5 sec and the gray screen for imagination is displayed for 2.5 sec. at a random time after the gray screen the subject were asked to give feedback whether they were able to vividly imagine the images or not. The images in this step are shown in the same order as in the first step. All images were displayed one time without repetition.

3.2.6. Signal screening and preprocessing

Prior to analyzing brain signals all recordings were screened by the patient's epileptologist. Recording sites were excluded if they were in close proximity to a locus with seizure-related activity, or if they were corrupted by large artifacts obviously not related to healthy brain activity. We also excluded recording sites located above the surface of the brain, as identified by inspecting the post-op structural images (MRI). A total of 251 out of 1342 recording sites were excluded based on these criteria.

After screening, all signals were referenced to a global mean. That is, for each subject independently a global average time-series was computed and subtracted from the time-series of each individual recording site.

3.2.7. Peri-stimulus power spectral density functions

For each recording site, the LFP starting from stimulus onset and ending 2 sec after was extracted and used to estimate a PSD (power spectral density) function (Miller et al., 2014; Miller et al., 2016). PSD frequencies ranged from 1Hz (DC offset was excluded) to 100Hz with increment of 1Hz; frequencies between 56 and 63Hz were excluded to compensate for a 60Hz line artifact. Each of these single-trial PSDs were normalized by calculating the logarithmic value of dividing single-trial PSDs over the mean power of all single-trial PSDs (Miller et al., 2016). Single-trial PSDs for each recording site were then grouped according to the task condition (i.e., vision prior to ISI, ISI, vision prior to MI, and MI) and averaged to construct a condition-specific average PSD. For each recording

site this process resulted in four condition-specific average PSD functions. Thus, a total of 4364 condition-specific PSDs were calculated from 1091 recording site across 13 subjects.

3.2.8. Principal Component Analysis

The 4364 PSDs were treated as independent 93-dimensional (one dimension for each of the frequencies in the PSD) observation vectors in a principal component analysis (PCA). This resulted in 93 orthogonal spectral components. Each spectral component was itself a 93-dimensional PSD function, with each value representing the modulation of power at each of the studied 93 frequency points. In this work we study the top 3 components, which accounted for roughly 50% of the variance. (**Figure 3.3**)

3.2.9. PC-specific encoding models

We investigated how variations in spectral power along each PC encoded information about variation in task conditions by constructing PC-specific encoding models. Encoding models were constructed independently for each recording site and subject. To construct models for subject k we first applied PCA to the PSDs from the other 12 subjects. We then projected the *single-trial* PSDs for subject k onto the first, second, and third PCs resulting from this subject-specific PCA. Thus, for each recording site we have 180 projections (one per experimental stimulus) per PC describing variation in spectral power along the PC. These projections are the "responses" that are predicted by each PC-specific encoding model. Formally, for a single recording site and subject let q_i be the PSD calculated for trial i, and let p_j be the jth principal component. Then $r_{ij} = q_i \cdot p_j$ is the single-trial response for PC_j that is predicted by each encoding model. The

encoding model for a single recording site in subject k is specified as a simple linear combination of task conditions:

$$r_j = Sw^T + b + \varepsilon$$

where r_j is an ($N_{train} \times 1$) vector of "responses" along PC_j, S is the ($N_{train} \times 4$) design matrix of the experiment (each column indicates a task condition), w is (4×1) vector of condition weights (i.e., regression parameters), b is an intercept term, and is zero-mean Gaussian noise. The number N_{train} indicates the number of training samples.

The values of the encoding model weights w and intercept b were determined for each recording site via simple linear regression. Regressions were performed by applying a *10-fold leave-k-out* procedure to a subset of *144* trials that used only for training and evaluating encoding models (the remaining N_{val}= 36 trials were used for decoding analyses as described below). This means that for each recording site, *10* separate regressions were performed. Each regression used a different set of $N_{train} = 116$ trials that were randomly sampled from the *144* trials used to construct encoding models. On each of these *10* folds, the regression model was evaluated on the remaining $N_{test} = 28$ trials. We used Pearson correlation between model predictions and the observed responses r_j. The "prediction accuracy" that we report for each encoding model is the average Pearson correlation across all *10* folds. Here an encoding model is considered "accurate" if the Pearson correlation exceeds a significance threshold ($p < .05$) determined by a random permutation test (permutation across trials of prediction and observed responses). The encoding model weights that we discuss and analyze below are the average of the weights across all *10* folds.

3.2.10. Model-based decoding analysis

A decoding analysis was performed on the $N_{val} = 36$ trials that were not used to estimate or evaluate the encoding models. Decoding analyses were performed using data from subjects S8-S13 only, as these were the subjects for which the common number of trials (consisting of *180* trials) was acquired.

Here, the decoding objective is to predict the visual mental state associated with a set of responses sampled from a population of recording sites. Decoding is performed independently for each PC. As above, a "response" r_j associated with the jth PC, $\boldsymbol{p}_j$ is defined as the projection of a PSD $\boldsymbol{q}$ onto the PC, $r_j = \boldsymbol{q} \cdot \boldsymbol{p}_j$. Below we will suppress the subscript j, as it is understood that all responses refer to a specific PC.

Let *s1, s2, s3, s4* indicate the visual mental states stimuli of "vision prior to ISI", "ISI", "vision prior to MI", and "MI", respectively. To decode the visual mental states for a given trial belonging to one of the visual states, for example *s3,* we first form a response vector r_{s3} associated with mental state of stimulus *s3*. We then concatenate the response to this trial across all recording sites. Thus

$$\boldsymbol{r}_{s3} = (r_{s3}^1, r_{s3}^2, \dots, r_{s3}^M)$$

where the superscript indexes a recording site, *M* is the total number of recording sites in the population, and the notation *s3* indicates a trial associated with the visual mental state "vision prior to MI". The length of a response vector for a given stimulus is thus $1 \times M$.

To perform model-based decoding of a visual mental state stimuli from a response vector, say r_{s3}, we use the encoding model for each recording site in the response vector to generate a *predicted response vector* $r'_{s1}, r'_{s2}, r'_{s3}, r'_{s4}$ for each of the 4 possible stimulus categories. We then calculate a Pearson correlation between the response vector

r_{s3}, and each of the predicted response vectors r'_{s1}, r'_{s2}, r'_{s3}, r'_{s4}. Decoding is successful if the correlation between the response vector and its matching *predicted* response vector is higher than the correlation the between response vectors and the other three, non-matching, predicted response vectors. We refer to successful decoding of a response vector as a "hit".

Decoding performance is the number of "hits" and divided by the total number of response vectors. Chance performance is 25%, since each response vector has a 1/4 chance of being successfully decoded by randomly the visual mental state. Decoding performance for visual mental state stimulus was calculated independently each PC.

As shown in **Figure 3.3**, decoding performance was calculated for across populations of varying sizes (i.e., populations with varying numbers of recording sites), from 2 to 489. To select recording sites for a population of a given size all recording sites were rank-ordered according to their prediction accuracy. Thus, the population of size 2 contained the recording sites with the highest and second-highest prediction accuracy, and so on. We emphasize that **none** of the trials used to measure prediction accuracy were used to measure decoding performance.

3.2.11. Statistical analysis

Statistical analyses were performed using MATLAB 2018b (Mathworks, MA) and Graphpad Prism 8 (GraphPad Software, CA). Permutation tests were performed for enrichment analyses and comparisons to random distributions. PCA analysis was performed as described above. One-sample t-test was used to compare accuracy of decoding models to random, and student's t-test was used to compare accuracy of decoding

between vision and attention. Unless otherwise specified, statistical significance is reported at alpha < 0.05.

3.3. Results

3.3.1. Broadband, gamma, and narrowband low frequency components explain almost half the variance in spectral power across visual mental states

To determine the combinations of frequency bands that explain the most variance in spectral power across visual mental states, we first prepared single-trial, peri-stimulus power spectral density functions (PSD) for each recording site in the dataset (1091 number of recording sites across 13 subjects). Single-trial PSDs were normalized (log(PSD/<PSD>)), where <> indicates an average across all trials for the given recording site; (Miller et al., 2016)). Normalized PSDs were then grouped according to their visual mental state category associated with each trial, and then averaged within-group. This resulted in 4 normalized mean PSDs.

PCA analysis was performed on pooled data from all subjects except test set as described in the methods. We found that variance was rather broadly distributed across PCs, with the first three PCs accounting for less than half (48.66 %) of the total variance in spectral power (**Figure 3.3**). PC1 (33.16 % of total variance) had a broadband spectral pattern represented by an elevation in power across all the studied frequency range (1-100 Hz). PC2 (10.18 %) corresponds to gamma band (high pass filter) pattern, and PC3 (5.32 %) corresponded to narrowband low frequency (low pass filter) spectral pattern represented by an elevation in power over a narrow frequency range. Specifically, PC2 distributes most

non-zero power in γ frequency range (above 50 Hz). PC3 distributed non-zero power primarily with $\delta - \beta$ frequency range (1-30 Hz). The PCA analysis reveals the main variation in power at each frequency across the different visual mental states. Notably, for each studied subject, we applied PCA analysis on all the PSDs from all other subjects while excluding recording sites from the studied subject.

A **B**
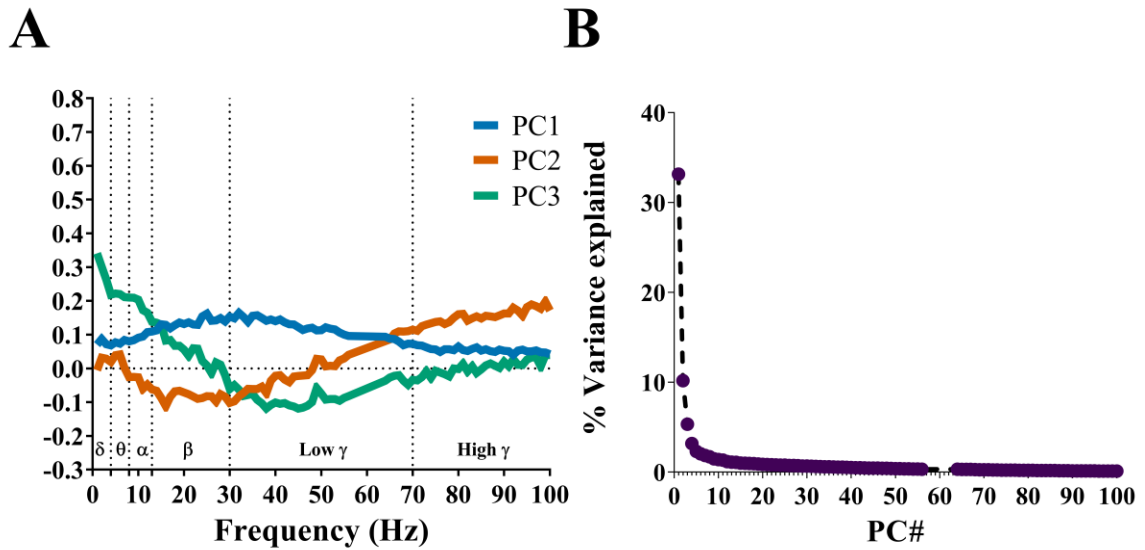
Figure 3.3. Principal component analysis of power spectral variation across visual mental states.
Left panel: PCA analysis applied to all condition-specific PSDs showing the spectral variance across conditions for subject S1. The top three PCs are used in our encoding model and are therefore calculated for each subject only using data from the remaining 12 subjects. The shown plot represents the PCA analysis on data from S2-13 used in the encoding model for subject S1. Results of PCA analysis shows PC1 (blue) with a broadband spectral pattern compared to PC2 (orange) that demonstrate a gamma band activity, and PC3 (green) that demonstrate low frequency spectral patterns. Right panel: percentage variance explained across PCs shows that PC1 has the highest percentage variance explained (33.16 % of total variance), then PC2(10.18 %), then PC3(5.32 %). After PC3 the percentage variance explained drops to less than 4%.

3.3.2. Broadband, gamma, and narrowband low frequency components encode visual mental states over a widely distributed brain network

In order to determine how information about visual mental states is encoded in each principal component, we independently estimated an encoding model for each of the first three PCs, and for each recording site. The encoding models used here were simple: for each PC and recording site, a design matrix (independent variable) indicating the visual mental state associated with each trial was regressed onto the recording site's projection onto the PC. Thus, the encoding model predicts, for each trial, the spectral power along each PC as a function of the stimulus category associated with the trial. We estimated encoding models independently for each PC and recording site using linear regression. We evaluated the prediction accuracy of the encoding model for each recording site and PC by calculating the Pearson correlation between the model's predictions and the observed spectral power along the PC across a held-out set of testing trials (**Figure 3.4**).

Accurately encoding recording sites were identified using a permutation test for the recording site-specific accuracy over 5000 iterations. Selection of accurately encoding recording sites was based on p-value<0.05, and the minimum correlation coefficient observed in these recording sites was 0.2 (**Figure 3.4 A-C** top panels). Accurately encoding recording sites across all three PCs were identified in the temporal, prefrontal, occipital, insular and parietal cortex (**Figure 3.4 A-C** bottom panels). There were no recording sites within the precentral gyrus that showed accurate encoding at any of the 3 PCs (0/7 studied recording sites). We observed significantly fewer accurately encoding recording sites for

PC1 (n=217) compared to PC2 (n=280), and significantly fewer accurately encoding recording sites for PC3 (n=118) compared to PC1 and to PC2.
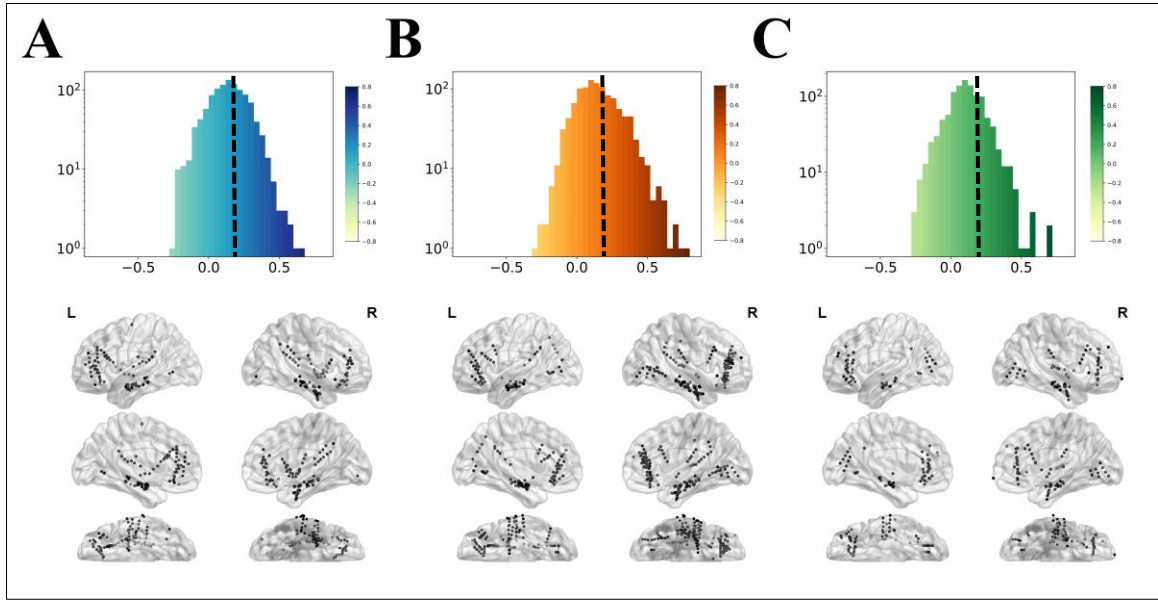
Figure 3.4. Spatial distribution of accurate recording sites encoding of PC1-3 projections across the studied 1091 recording sites

Encoding model described in section 3.2.9 is applied to all studied 1091 recording sites across all three studied PCs (PC1-PC3). Top panels: Histogram illustrating the distribution of recording sites by encoding accuracy for PC in log-scale (PC1 in blue, PC2 in orange, PC3 in green). The dashed line represents the accuracy threshold used to define accurately encoding recording sites. Bottom panels: the spatial distribution of accurately encoding recording sites represents the anatomical distribution in the human brain presented in the MNI space across the 13 subjects for PC1 (**A,** N=217 recording sites), PC2 (**B,** N=280 recording sites), and PC3 (**C,** N=118 recording sites). L: Left hemisphere, R: Right hemisphere.

3.3.3. Gamma band decodes all four visual mental states the best compared to broadband and low frequency patterns

Using the decoding approach described in section 3.2.10, we found that gamma band decodes the studied four visual mental states the best when compared to broadband PC1, and narrowband low frequency PC3 with accuracy that reaches 90% when adding more recording sites to the decoding model. PC2 reaches high decoding accuracy from the first 3 studied recording sites (>75%), whereas PC1 and PC3 reach high decoding accuracy at around 100 and 50 recording sites respectively (**Figure 3.5**).
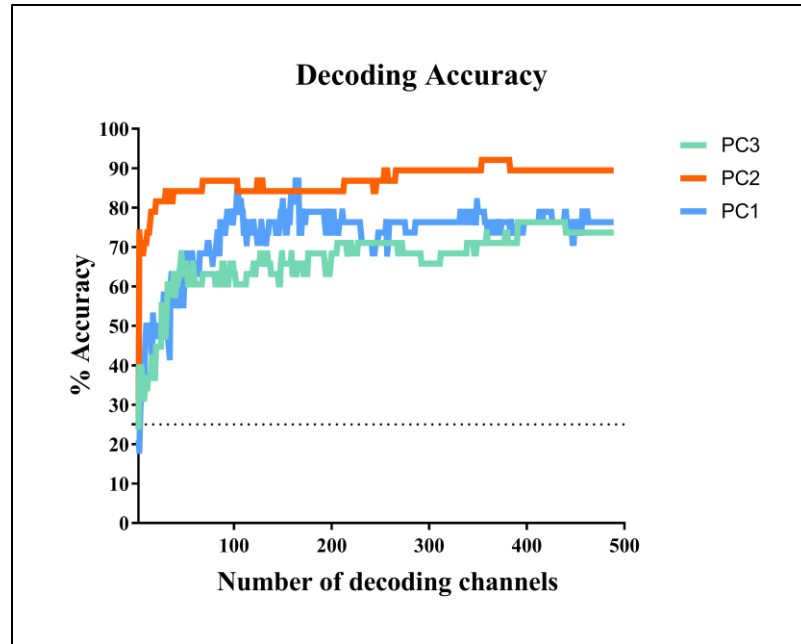
Figure 3.5 Decoding accuracy of studied visual mental states for PC1, PC2, and PC3

Plot representing the decoding accuracy as function of increasing number of decoding recording sites in all 489 for each PC. Broadband PC1 pattern (blue) decodes the four studied visual mental states with low accuracy when studied over a small group of decoding recording sites, but it increases and reach a plateau of around 70% when the number of the studied recording sites is around 100. PC2 (orange) gamma high frequency decodes the best for all four visual mental states with the decoding accuracy jumping to 75% from the first 3 decoding recording sites and reaching 90% with the increase of number of decoding recording sites. PC3 (green) narrowband low frequency pattern accurately decode the visual mental states when using more than 50 decoding recording sites at a time and reaches a percentage accuracy in the 60-70% range.

3.3.4. Broadband, and low frequency decode best for passive and attentive vision, while gamma decodes the best for attentive vision and mental imagery

We then studied the confusion matrix representing the detailed decoding accuracy of each of the four visual mental states over the first three PCs (**Figure 3.6**). We found that broadband PC1, and low frequency PC3 had the highest decoding accuracy for passive and attentive vision (~80%), and the lowest for ISI and MI (50-55%), whereas gamma band high frequency PC2 pattern, decoded attentive vision and MI without any error (100%), and passive vision with ~90%. Gamma decodes had the lowest decoding accuracy for ISI.
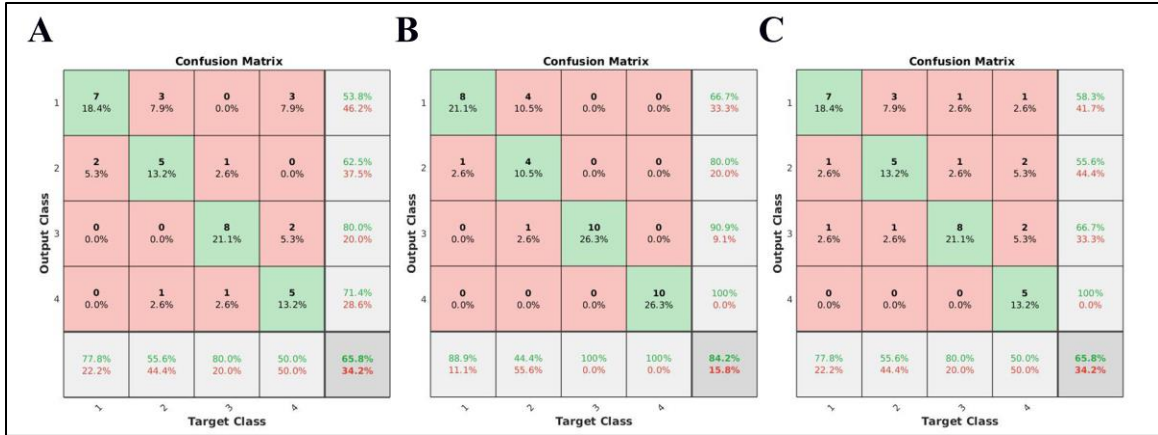
Figure 3.6. Confusion matrices showing accuracy of decoding of the four visual mental states using PC1-3

Shown is the confusion matrix for one instance of the decoding accuracy calculated when the first best 100 encoding recording sites for the corresponding studied PC are used in the decoding. For all three tables the numbers 1 to 4 on the target and output classes represent in the order: passive vision, ISI, attentive vision, and MI. The rows represent the output predicted class, and the columns represent the actual class (or target class). The cells in the diagonal represents the accurately classified trials. The off-diagonal cells are the incorrectly classified trials. In each cell the number of trials and their percentage of the total number of trials is shown. The last column on the right of each table represent the precision (positive predictive value in green), and false discovery rate (in red). The row at the bottom of each table shows the percentage of correctly classified trials also called recall or true positive rate (green), and the percentage of incorrectly classified trials or false negative rate (red). The last cell in the lower right corner represents the overall accuracy. **A-C:** Confusion matrix of PC1 broadband pattern **(A)**, PC2 gamma band **(B)**, and PC3 low frequency **(C)** show that broadband and low frequency spectral patterns decodes the best for passive vision and attentive vision (~80%), and the least to ISI and MI (50-55%), and gamma band decodes the best for attentive vision and MI.

3.4. Discussion

In this chapter, we studied the visual mental state in the brain by changing the task and the seen stimuli among passive viewing of images of paintings (abstract, landscape, and face), ISI, attentive viewing of paintings, and mental imagery of the attended paintings. We studied how the different visual mental states are encoded in the brain at the spectral level. We found that broadband, low frequency (<30 Hz), and gamma band (>30 Hz) frequency represent the most variance explained across the studied four visual mental states across 1091 recording sites in 13 participants. Our finding of increase of power in the gamma band support what was reported about maintenance of mental imagery in working memory and recall to be spectrally associated with increase of gamma activity (30-100Hz) (Jensen et al., 2007) when studied using MEG, EEG, and LFP recordings (Sederberg et al., 2003; Gruber et al., 2004; Osipova et al., 2006; Sederberg et al., 2007). Moreover, the increase of power in the low frequency PC3 component support the reported theta (Sauseng et al., 2010) and alpha oscillations (Jokisch and Jensen, 2007) were also reported to be increased along with the increase of memory load. The importance of this study is that it showed the wide distribution of recording sites encoding for visual mental state across different brain regions, consistent with the pattern shown with fMRI studies (Ganis et al., 2004; Dijkstra et al., 2017).

The decoding accuracy of gamma band was the highest compared to broadband and narrowband. This emphasizes the role of gamma in decoding the studied visual mental states, especially that gamma had higher accuracy when decoding for attentive vision and mental imagery compared to passive vision, and as the lowest for ISI. This means that gamma is mostly involved when the brain is memorizing and recalling visual images, and

during processing of vision. Those results are consistent with the findings discussed in **Chapter 2**, where we showed that during category-based visual attention, gamma band did not stand as a separate component when PCA was applied to the spectra of seen/attended categories. Although our earlier results do not mean that gamma is not involved in category-based visual attention, but rather they indicated that gamma did not stand as a separate component to be represented in the first three PCs. One of the explanations of why gamma did not explain significant variability in our prior experiment compared to our current work is likely that gamma was increasing consistently with all stimuli in our prior experiment of seen/attended object category variation. PCA analysis reflects the variance across the studied stimuli, so if gamma increase in a consistent manner for the studied stimuli, then gamma would not stand out as one of the differentially modulated spectral patterns. In the experiments performed in **Chapter 2**, attention was a common factor across all stimuli. Even during ISI, participants were keeping the category of the last seen image in mind to give an answer about recalling the last image. This prior design in Chapter 2 is similar to the second phase of this study where the studied states are attentive vision and mental imagery. In order to test whether gamma would be majorly modulated between spectra of attentive vision and mental imagery, we applied PCA to only those two visual mental states instead of all four and the results were, indeed, consistent with those seen in Chapter 2. Specifically, we show the prominent contribution to variance by a broadband effect, a low frequency narrowband (<10 Hz), and a low frequency alpha-beta band (10-30 Hz) (data not shown).

Interestingly, the fact that gamma decoding was accurate even with a small number of recording sites (3 recording sites) support the hypothesis that gamma reflects local

reverberant circuitries in the brain (Miller et al., 2014), where almost single units (recording sites) are keeping information about the visual mental states. On the other hand, broadband and low frequency narrowband decoders were mostly accurate for vision, regardless of if it was passive or attentive viewing of images. Collectively, our findings indicate the visual processing in the brain involved both broadband and low frequency narrowband patterns; however, the gamma band is specifically involved in the memorization and recall of observed and imagined objects or scenes.

A potential future extension of this work is to test the ability to use spectral based decoders to accurately decode specific object categories of visual mental imagery especially that the experiment was designed for participants to imagine three different categories (abstract, landscape, and faces). Another aspect of mental imagery to be explored is the difference between imagining abstract paintings, which most participants reported to be hard to accurately imagine, and other imagined object categories that are closer to natural scenes. It would be also interesting to compare the difference in attention while looking at abstract paintings that are hard to memorize versus scenes that can be relative easier in memorizing and imagining such as faces.

CHAPTER FOUR

SUMMARY OF FINDINGS

4. Summary

In summary and across **Chapters 2 and 3**, we have successfully implemented an unbiased spectral approach to study spectral encoding and decoding of various visual or visual related object categories, across widely distributed LFP recording sites, and we introduced encoding and decoding models that can be applied to any type of experiments studying the responses of LFP recordings across various stimuli. We also provided evidence on the contribution of different spectral frequency bands to different components of visual processing and visual mental imagery in the human brain.

What we have learned about the brain from all the results is multifold: First, broadband spectral pattern reflects the main variance in power across object-based visual tasks involving study of category-based visual attention and visual mental states in human brain. This broadband spectral pattern mainly decodes bottom-up sensory input regardless of whether it was passive or attentive viewing of photographs. Second, low frequency delta-theta band decodes the best for attention and vision. Third, low frequency alpha-beta band differentially decodes top-down attentional state better than vision. Fourth, gamma band decodes the best for memorization of attentively viewed images and recall of mental imagery.

Previous work reported some similar results to ours when studied in focal recording sites, but to our knowledge this is the first study that took an expansive spatial and spectral view to study feedforward and feedback processing of visual information in the human brain and set up the stage for a better understanding of the mechanisms by which visual information is encoded in the brain. The identified spectral patterns could be used

as biomarkers to sense visual mental states and could be targeted (stimulation/modulation) in potential therapeutic approaches in deficits and disorders affecting visual processing in the human brain.

References

Albers AM, Kok P, Toni I, Dijkerman HC, de Lange FP (2013) Shared representations for working memory and mental imagery in early visual cortex. Curr Biol 23:1427-1431.

Allison T, Puce A, Spencer DD, McCarthy G (1999) Electrophysiological studies of human face perception. I: Potentials generated in occipitotemporal cortex by face and non-face stimuli. Cereb Cortex 9:415-430.

Andersson P, Pluim JP, Siero JC, Klein S, Viergever MA, Ramsey NF (2011) Real-time decoding of brain responses to visuospatial attention using 7T fMRI. PLoS One 6:e27638.

Ashby FG, Maddox WT (2005) Human category learning. Annu Rev Psychol 56:149-178.

Bar M, Tootell RB, Schacter DL, Greve DN, Fischl B, Mendola JD, Rosen BR, Dale AM (2001) Cortical mechanisms specific to explicit visual object recognition. Neuron 29:529-535.

Bartolomeo P (2008) The neural correlates of visual mental imagery: an ongoing debate. Cortex 44:107-108.

Bartolomeo P, Bourgeois A, Bourlon C, Migliaccio R (2013) Visual and motor mental imagery after brain damage. In: Multisensory Imagery, pp 249-269: Springer.

Bastos AM, Vezoli J, Bosman CA, Schoffelen JM, Oostenveld R, Dowdall JR, De Weerd P, Kennedy H, Fries P (2015) Visual areas exert feedforward and feedback influences through distinct frequency channels. Neuron 85:390-401.

Bosman CA, Schoffelen JM, Brunet N, Oostenveld R, Bastos AM, Womelsdorf T, Rubehn B, Stieglitz T, De Weerd P, Fries P (2012) Attentional stimulus selection through selective synchronization between monkey visual areas. Neuron 75:875-888.

Brett M, Leff AP, Rorden C, Ashburner J (2001) Spatial normalization of brain images with focal lesions using cost function masking. Neuroimage 14:486-500.

Brunet N, Vinck M, Bosman CA, Singer W, Fries P (2014) Gamma or no gamma, that is the question. Trends Cogn Sci 18:507-509.

Buffalo EA, Fries P, Landman R, Buschman TJ, Desimone R (2011) Laminar differences in gamma and alpha coherence in the ventral stream. Proc Natl Acad Sci U S A 108:11262-11267.

Chao LL, Haxby JV, Martin A (1999) Attribute-based neural substrates in temporal cortex for perceiving and knowing about objects. Nat Neurosci 2:913-919.

Cukur T, Nishimoto S, Huth AG, Gallant JL (2013) Attention during natural vision warps semantic representation across the human brain. Nat Neurosci 16:763-770.

Damasio AR, Damasio H, Van Hoesen GW (1982) Prosopagnosia: anatomic basis and behavioral mechanisms. Neurology 32:331-341.

David SV, Hayden BY, Mazer JA, Gallant JL (2008) Attention to stimulus features shifts spectral tuning of V4 neurons during natural vision. Neuron 59:509-521.

Davidesco I, Harel M, Ramot M, Kramer U, Kipervasser S, Andelman F, Neufeld MY, Goelman G, Fried I, Malach R (2013) Spatial and object-based attention modulates broadband high-frequency responses across the human visual cortical hierarchy. J Neurosci 33:1228-1240.

De Vreese LP (1991) Two systems for colour-naming defects: verbal disconnection vs colour imagery disorder. Neuropsychologia 29:1-18.

Del Cul A, Baillet S, Dehaene S (2007) Brain dynamics underlying the nonlinear threshold for access to consciousness. PLoS Biol 5:e260.

Desimone R, Albright TD, Gross CG, Bruce C (1984) Stimulus-selective properties of inferior temporal neurons in the macaque. J Neurosci 4:2051-2062.

Dijkstra N, Bosch SE, van Gerven MA (2017) Vividness of Visual Imagery Depends on the Neural Overlap with Perception in Visual Areas. J Neurosci 37:1367-1373.

Duncan J (2001) An adaptive coding model of neural function in prefrontal cortex. Nat Rev Neurosci 2:820-829.

Fallgatter AJ, Mueller TJ, Strik WK (1997) Neurophysiological correlates of mental imagery in different sensory modalities. Int J Psychophysiol 25:145-153.

Farah MJ (1984) The neurological basis of mental imagery: a componential analysis. Cognition 18:245-272.

Farah MJ (1988) Is visual imagery really visual? Overlooked evidence from neuropsychology. Psychol Rev 95:307-317.

Felleman DJ, Van Essen DC (1991) Distributed hierarchical processing in the primate cerebral cortex. Cereb Cortex 1:1-47.

Fisch L, Privman E, Ramot M, Harel M, Nir Y, Kipervasser S, Andelman F, Neufeld MY, Kramer U, Fried I, Malach R (2009) Neural "ignition": enhanced activation linked to perceptual awareness in human ventral stream visual cortex. Neuron 64:562-574.

Fries P (2009) Neuronal gamma-band synchronization as a fundamental process in cortical computation. Annu Rev Neurosci 32:209-224.

Fries P, Scheeringa R, Oostenveld R (2008) Finding gamma. Neuron 58:303-305.

Fries P, Reynolds JH, Rorie AE, Desimone R (2001) Modulation of oscillatory neuronal synchronization by selective visual attention. Science 291:1560-1563.

Fylan F, Holliday IE, Singh KD, Anderson SJ, Harding GF (1997) Magnetoencephalographic investigation of human cortical area V1 using color stimuli. Neuroimage 6:47-57.

Gaillard R, Dehaene S, Adam C, Clemenceau S, Hasboun D, Baulac M, Cohen L, Naccache L (2009) Converging intracranial markers of conscious access. PLoS Biol 7:e61.

Ganis G, Thompson WL, Kosslyn SM (2004) Brain areas underlying visual mental imagery and visual perception: an fMRI study. Brain Res Cogn Brain Res 20:226-241.

Gilbert CD, Li W (2013) Top-down influences on visual processing. Nat Rev Neurosci 14:350-363.

Gomez Gonzalez CM, Clark VP, Fan S, Luck SJ, Hillyard SA (1994) Sources of attention-sensitive visual event-related potentials. Brain Topogr 7:41-51.

Goodale MA, Milner AD (1992) Separate visual pathways for perception and action. Trends Neurosci 15:20-25.

Gruber T, Tsivilis D, Montaldi D, Muller MM (2004) Induced gamma band responses: an early marker of memory encoding and retrieval. Neuroreport 15:1837-1841.

Harmony T (2013) The functional significance of delta oscillations in cognitive processing. Front Integr Neurosci 7:83.

Haxby JV, Gobbini MI, Furey ML, Ishai A, Schouten JL, Pietrini P (2001) Distributed and overlapping representations of faces and objects in ventral temporal cortex. Science 293:2425-2430.

Helfrich RF, Huang M, Wilson G, Knight RT (2017) Prefrontal cortex modulates posterior alpha oscillations during top-down guided visual perception. Proc Natl Acad Sci U S A 114:9457-9462.

Hermes D, Nguyen M, Winawer J (2017) Neuronal synchrony and the relation between the blood-oxygen-level dependent response and the local field potential. PLoS Biol 15:e2001461.

Hermes D, Miller KJ, Wandell BA, Winawer J (2015) Stimulus Dependence of Gamma Oscillations in Human Visual Cortex. Cereb Cortex 25:2951-2959.

Herzog MH, Clarke AM (2014) Why vision is not both hierarchical and feedforward. Front Comput Neurosci 8:135.

Hoogenboom N, Schoffelen JM, Oostenveld R, Parkes LM, Fries P (2006) Localizing human visual gamma-band activity in frequency, time and space. Neuroimage 29:764-773.

Hubel DH, Wiesel TN (1959) Receptive fields of single neurones in the cat's striate cortex. J Physiol 148:574-591.

Hubel DH, Wiesel TN (1961) Integrative action in the cat's lateral geniculate body. J Physiol 155:385-398.

Hubel DH, Wiesel TN (1962) Receptive fields, binocular interaction and functional architecture in the cat's visual cortex. J Physiol 160:106-154.

Ikkai A, Dandekar S, Curtis CE (2016) Lateralization in Alpha-Band Oscillations Predicts the Locus and Spatial Distribution of Attention. PLoS One 11:e0154796.

Ishai A, Ungerleider LG, Haxby JV (2000) Distributed neural systems for the generation of visual images. Neuron 28:979-990.

Isik L, Singer J, Madsen JR, Kanwisher N, Kreiman G (2018) What is changing when: Decoding visual information in movies from human intracranial recordings. Neuroimage 180:147-159.

Jacobs J, Kahana MJ (2009) Neural representations of individual stimuli in humans revealed by gamma-band electrocorticographic activity. J Neurosci 29:10203-10214.

Jensen O, Kaiser J, Lachaux JP (2007) Human gamma-frequency oscillations associated with attention and memory. Trends Neurosci 30:317-324.

Jensen O, Bonnefond M, Marshall TR, Tiesinga P (2015) Oscillatory mechanisms of feedforward and feedback visual processing. Trends Neurosci 38:192-194.

Jia X, Xing D, Kohn A (2013) No consistent relationship between gamma power and peak frequency in macaque primary visual cortex. J Neurosci 33:17-25.

Jokisch D, Jensen O (2007) Modulation of gamma and alpha activity during a working memory task engaging the dorsal or ventral stream. J Neurosci 27:3244-3251.

Joseph JE (2001) Functional neuroimaging studies of category specificity in object recognition: a critical review and meta-analysis. Cogn Affect Behav Neurosci 1:119-136.

Kafaligonul H, Breitmeyer BG, Ogmen H (2015) Feedforward and feedback processes in vision. Front Psychol 6:279.

Kanwisher N, McDermott J, Chun MM (1997) The fusiform face area: a module in human extrastriate cortex specialized for face perception. J Neurosci 17:4302-4311.

Klimesch W (1999) EEG alpha and theta oscillations reflect cognitive and memory performance: a review and analysis. Brain Res Brain Res Rev 29:169-195.

Klimesch W, Fellinger R, Freunberger R (2011) Alpha oscillations and early stages of visual encoding. Front Psychol 2:118.

Kosslyn SM, Ganis G, Thompson WL (2001) Neural foundations of imagery. Nat Rev Neurosci 2:635-642.

Kourtzi Z, Connor CE (2011) Neural representations for object perception: structure, category, and adaptive coding. Annu Rev Neurosci 34:45-67.

Kraskov A, Quiroga RQ, Reddy L, Fried I, Koch C (2007) Local field potentials and spikes in the human medial temporal lobe are selective to image category. J Cogn Neurosci 19:479-492.

Kreiman G, Koch C, Fried I (2000a) Imagery neurons in the human brain. Nature 408:357-361.

Kreiman G, Koch C, Fried I (2000b) Category-specific visual responses of single neurons in the human medial temporal lobe. Nat Neurosci 3:946-953.

Kunimatsu J, Maeda K, Hikosaka O (2019) The Caudal Part of Putamen Represents the Historical Object Value Information. J Neurosci 39:1709-1719.

Levine DN, Warach J, Farah M (1985) Two visual systems in mental imagery: dissociation of "what" and "where" in imagery disorders due to bilateral posterior cerebral lesions. Neurology 35:1010-1018.

Liu J, Harris A, Kanwisher N (2002) Stages of processing in face perception: an MEG study. Nat Neurosci 5:910-916.

Majima K, Matsuo T, Kawasaki K, Kawai K, Saito N, Hasegawa I, Kamitani Y (2014) Decoding visual object categories from temporal correlations of ECoG signals. Neuroimage 90:74-83.

Manning JR, Jacobs J, Fried I, Kahana MJ (2009) Broadband shifts in local field potential power spectra are correlated with single-neuron spiking in humans. J Neurosci 29:13613-13620.

Markov NT, Vezoli J, Chameau P, Falchier A, Quilodran R, Huissoud C, Lamy C, Misery P, Giroud P, Ullman S, Barone P, Dehay C, Knoblauch K, Kennedy H (2014) Anatomy of hierarchy: feedforward and feedback pathways in macaque visual cortex. J Comp Neurol 522:225-259.

Michalareas G, Vezoli J, van Pelt S, Schoffelen JM, Kennedy H, Fries P (2016) Alpha-Beta and Gamma Rhythms Subserve Feedback and Feedforward Influences among Human Visual Cortical Areas. Neuron 89:384-397.

Miller KJ (2015) The dynamics of category-specific perception in ventral temporal cortex. In.

Miller KJ, Sorensen LB, Ojemann JG, den Nijs M (2009a) Power-law scaling in the brain surface electric potential. PLoS Comput Biol 5:e1000609.

Miller KJ, Zanos S, Fetz EE, den Nijs M, Ojemann JG (2009b) Decoupling the cortical power spectrum reveals real-time representation of individual finger movements in humans. J Neurosci 29:3132-3137.

Miller KJ, Schalk G, Hermes D, Ojemann JG, Rao RP (2016) Spontaneous Decoding of the Timing and Content of Human Object Perception from Cortical Surface Recordings Reveals Complementary Information in the Event-Related Potential and Broadband Spectral Change. PLoS Comput Biol 12:e1004660.

Miller KJ, Schalk G, Fetz EE, den Nijs M, Ojemann JG, Rao RP (2010a) Cortical activity during motor execution, motor imagery, and imagery-based online feedback. Proc Natl Acad Sci U S A 107:4430-4435.

Miller KJ, Honey CJ, Hermes D, Rao RP, denNijs M, Ojemann JG (2014) Broadband changes in the cortical surface potential track activation of functionally diverse neuronal populations. Neuroimage 85 Pt 2:711-720.

Miller KJ, Hermes D, Honey CJ, Sharma M, Rao RP, den Nijs M, Fetz EE, Sejnowski TJ, Hebb AO, Ojemann JG, Makeig S, Leuthardt EC (2010b) Dynamic modulation of local population activity by rhythm phase in human occipital cortex during a visual search task. Front Hum Neurosci 4:197.

Moran J, Desimone R (1985) Selective attention gates visual processing in the extrastriate cortex. Science 229:782-784.

O'Craven KM, Downing PE, Kanwisher N (1999) fMRI evidence for objects as the units of attentional selection. Nature 401:584-587.

Osipova D, Takashima A, Oostenveld R, Fernandez G, Maris E, Jensen O (2006) Theta and gamma oscillations predict encoding and retrieval of declarative memory. J Neurosci 26:7523-7531.

Pearson J, Naselaris T, Holmes EA, Kosslyn SM (2015) Mental Imagery: Functional Mechanisms and Clinical Applications. Trends Cogn Sci 19:590-602.

Peelen MV, Fei-Fei L, Kastner S (2009) Neural mechanisms of rapid natural scene categorization in human visual cortex. Nature 460:94-97.

Penfield W, Perot P (1963) The Brain's Record of Auditory and Visual Experience. A Final Summary and Discussion. Brain 86:595-696.

Pfurtscheller G, Lopes da Silva FH (1999) Event-related EEG/MEG synchronization and desynchronization: basic principles. Clin Neurophysiol 110:1842-1857.

Pfurtscheller G, Neuper C, Mohl W (1994) Event-related desynchronization (ERD) during visual processing. Int J Psychophysiol 16:147-153.

Ramot M, Fisch L, Harel M, Kipervasser S, Andelman F, Neufeld MY, Kramer U, Fried I, Malach R (2012) A widely distributed spectral signature of task-negative electrocorticography responses revealed during a visuomotor task in the human cortex. J Neurosci 32:10458-10469.

Ray S, Maunsell JH (2010) Differences in gamma frequencies across visual cortex restrict their possible use in computation. Neuron 67:885-896.

Rorden C, Hanayik T (2014) StimSync: open-source hardware for behavioral and MRI experiments. J Neurosci Methods 227:90-99.

Rorden C, Bonilha L, Fridriksson J, Bender B, Karnath HO (2012) Age-specific CT and MRI templates for spatial normalization. Neuroimage 61:957-965.

Sauseng P, Griesmayr B, Freunberger R, Klimesch W (2010) Control mechanisms in working memory: a possible function of EEG theta oscillations. Neurosci Biobehav Rev 34:1015-1022.

Schifferstein HN (2009) Comparing mental imagery across the sensory modalities. Imagination, Cognition and Personality 28:371-388.

Schmolesky MT, Wang Y, Hanes DP, Thompson KG, Leutgeb S, Schall JD, Leventhal AG (1998) Signal timing across the macaque visual system. J Neurophysiol 79:3272-3278.

Sederberg PB, Kahana MJ, Howard MW, Donner EJ, Madsen JR (2003) Theta and gamma oscillations during encoding predict subsequent recall. J Neurosci 23:10809-10814.

Sederberg PB, Schulze-Bonhage A, Madsen JR, Bromfield EB, McCarthy DC, Brandt A, Tully MS, Kahana MJ (2007) Hippocampal and neocortical gamma oscillations predict memory formation in humans. Cereb Cortex 17:1190-1196.

Tallon-Baudry C, Bertrand O, Delpuech C, Permier J (1997) Oscillatory gamma-band (30-70 Hz) activity induced by a visual search task in humans. J Neurosci 17:722-734.

Thut G, Nietzel A, Brandt SA, Pascual-Leone A (2006) Alpha-band electroencephalographic activity over occipital cortex indexes visuospatial attention bias and predicts visual target detection. J Neurosci 26:9494-9502.

van Gerven MA, Maris E, Sperling M, Sharan A, Litt B, Anderson C, Baltuch G, Jacobs J (2013) Decoding the memorization of individual stimuli with direct human brain recordings. Neuroimage 70:223-232.

VanRullen R, Thorpe SJ (2001) The time course of visual processing: from early perception to decision-making. J Cogn Neurosci 13:454-461.

Vidal JR, Ossandon T, Jerbi K, Dalal SS, Minotti L, Ryvlin P, Kahane P, Lachaux JP (2010) Category-Specific Visual Responses: An Intracranial Study Comparing Gamma, Beta, Alpha, and ERP Response Selectivity. Front Hum Neurosci 4:195.

Warden MR, Miller EK (2010) Task-dependent changes in short-term memory in the prefrontal cortex. J Neurosci 30:15801-15810.

Xing D, Yeh CI, Burns S, Shapley RM (2012) Laminar analysis of visually evoked activity in the primary visual cortex. Proc Natl Acad Sci U S A 109:13871-13876.

Yamamoto S, Monosov IE, Yasuda M, Hikosaka O (2012) What and where information in the caudate tail guides saccades to visual objects. J Neurosci 32:11005-11016.

Yeterian EH, Van Hoesen GW (1978) Cortico-striate projections in the rhesus monkey: the organization of certain cortico-caudate connections. Brain Res 139:43-63.

Appendix III

PUBLICATIONS

List of Publications

In preparation/under review

1- Sabra Z, Leonardo Bonilha, and Thomas Naselaris. "Encoding and decoding models of category-based visual attention in the human brain". *Under Review*.

2- Sabra Z, Leonardo Bonilha, and Thomas Naselaris. "Spectral encoding of mental imagery in human brain". *In Prep*.

Published manuscripts

1. Alawieh A, **Sabra Z**, Langley F, Bizri A, Hamadeh R, and Zaraket F. "Assessing the impact of the Lebanese National Polio Immunization Campaign using a population-based computational model". BMC Public Health 17.1 (2017): 902.

2. **Sabra Z** and Artail H. "Using group anonymity to hide the identity of VoIP mobile users communicating over hybrid networks while preserving quality of service". Wireless Communications and Mobile Computing (2016). 16(17), 2792-2808.

3. Alawieh A, **Sabra Z**, Bizri A, Davies C, White R, and Zaraket F. "A computational model to monitor and predict trends in bacterial resistance". Journal of Global Antimicrobial Resistance (2015) 3(3):174-183.

4. Alawieh A, Sabra M, **Sabra Z**, Tomlinson S, and Zaraket F. "Molecular Architecture of Spinal Cord Injury Protein Interaction Network". PLoS One (2015) 10(8):0135024.

5. Alawieh A, **Sabra Z**, Sabra M, Tomlinson S, and Zaraket F. "A rich-club organization in brain ischemia protein interaction network". Scientific Reports (2015) 5:13513.

6. **Sabra Z** and Artail H. "Preserving anonymity and quality of service for VoIP applications over hybrid networks". IEEE Mediterranean Electrotechnical Conference 2014. pp. 421-425

7. Dikmak M, **Sabra Z**, Kayssi A, and Chehab A. "Optimized conditional privacy preservation in VANETs". International Conference on Telecommunication (ICT) 2012. pp. 1-6.

8. Dikmak M, **Sabra Z**, and Artail H. "QoS-based mediated agent and intelligent requester for dynamic web service provision". International Conference on Telecommunication (ICT) 2012. pp. 1-6.

9. Hamady F, Sabra M, **Sabra Z**, Kayssi A, Chehab A, Mansour M. Enhancement of the S-MAC protocol for wireless sensor networks. In2010 International Conference on Energy Aware Computing 2010 Dec 16 (pp. 1-4). IEEE.

Book chapters

1. Alawieh A, **Sabra Z,** Zhang Z, Kobeissy F, Wang K. Neuroproteomics and Neurosystems Biology in the Quest of TBI Biomarker Discovery. In: Wang K, Zhang Z, Kobeissy F, editors. Biomarkers of CNS injury and Neurological Disorders: CRC Press; 2014.

2. Alawieh A, Zaraket F, **Sabra Z**, Mondello S, Kobeissy F. Bioinformatic approach to understanding interacting pathways in neuropsychiatric disorders. In: Trent R, editor. Clinical Bioinformatics: Springer; 2014.

3. Fadlallah B, Fadlallah A, Alawieh A, **Sabra Z**, El-Sayyad M, Kobeissy F. Robust Detection of Epilepsy using Weighted-Permutation Entropy: Methods and Analysis. In: Kastania AN, Jain L, editors. Advanced Computational Intelligence Paradigms in Healthcare: Springer-Verlag; 2014.

Appendix IV

ABSTRACTS

Abstracts

1. **Sabra Z**, Bonilha L, and Naselaris T. "The spatial and spectral distribution of visual information : an unbiased exploration using ECoG recordings in human brain". Society for Neuroscience Annual Meeting 2017. Washington, DC.

2. **Sabra Z**, Breedlove J, Bonilha L, and Naselaris T. "Oscillation-based Decoding of Visual Attentional and Perceptual Processes in the Hippocampus Using ECoG". MUSC Research Day 2016. Charleston, SC.

3. **Sabra Z**, Breedlove J, Bonilha L, and Naselaris T. "Representation of attentional and perceptual states during visualization of natural scenes". MUSC Research Day 2015. Charleston, SC.

4. **Sabra Z**, Breedlove J, Bonilha L, and Naselaris T. "The representation of semantic content and attentional state in medial temporal lobe during visual processing of natural scenes: an ECoG study". Society for Neuroscience Annual Meeting 2015. Chicago, IL.

5. Sabra M, Alawieh A, **Sabra Z**, Zaraket F, Hamadeh G. "Semi-automatic Annotator for Medical Natural Language Processing Applications (SAMNA)". American University of Beirut Research Day 2015. Beirut, Lebanon.

6. Alawieh A, Sabra M, **Sabra Z**, Zaraket F, and Tomlinson S. "A Rich Club Organization in Spinal Cord Injury Interactome Provides Insight into Pathophysiological Mechanisms and Potential Therapeutic Interventions". American Society for Clinical Investigation (ASCI) Annual Meeting 2015. Chicago, IL.

7. Alawieh A, **Sabra Z**, Sabra M, Tomlinson S, Zaraket F. "A Rich-club Organization of the Brain Ischemic meta-Proteome: Understanding Stroke Pathogenesis and Therapy Using Graph Theory". Perry V. Halushka MUSC Research Day 2014. Charleston, SC.

8. Alawieh A, **Sabra Z**, Sabra M, and Zaraket F. "Novel Bioinformatics Approach Reveals Pathogenic Mechanisms in Cerebral Ischemia - A Step towards Preclinical Stroke Information Management System". International Stroke Conference 2015. Nashville, TN.

Appendix IV

AWARDS

Research Funding

2013-2014   **2014 Farouk Jabre Award; $ 50,000**

Title: Using natural language processing for extraction of information from free-text in electronic medical records

Farouk Jabre Association through the American University of Beirut

Awards

2014   **Outstanding Scientific Research Proposal Award**

American University of Beirut